Modern speleothem oxygen isotope hydroclimate records in water-limited SE Australia

[1,2,3,4]Monika Markowska, [2,5]Mark O. Cuthbert, [2,3*]Andy Baker, [1,2]Pauline C. Treble, [2,6]Martin S. Andersen, [7]Lewis Adler, [1]Alan Griffiths, [8]Silvia Frisia.

[1]ANSTO, Lucas Heights, Sydney 2234, Australia

[2]Connected Waters Initiative Research Centre, UNSW Australia, Kensington, Sydney 2033, Australia.

[3]School of Biological, Earth and Environmental Sciences, UNSW Australia, Kensington, Sydney 2033, Australia.

[4]Faculty of Geosciences, Tübingen University, Tübingen, 72074, Germany

[5]School of Earth and Ocean Sciences, Cardiff University, Cardiff, CF10 3AT, UK

[6]School of Civil and Environmental Engineering, UNSW Australia, Kensington, Sydney 2033, Australia.

[7]Bioanalytical Mass Spectrometry Facility, Mark Wainwright Analytical Centre, UNSW Australia, Kensington, Sydney 2033, Australia.

[8]School of Environmental and Life Science, University of Newcastle, Callaghan NSW, 2308, Australia.

**Corresponding author: a.baker@unsw.edu.au*

Keywords: speleothems, water-limited climate, water isotopes, hydroclimate,

Abstract

Dryland regions are generally projected to become drier under future climate change scenarios. Understanding the long-term natural variability of dryland regions via paleo-reconstructions is therefore highly desirable. The $\delta^{18}O$ of two coeval modern speleothems from Cathedral Cave, Wellington, in semi-arid SE Australia are compared to the instrumental record to assess their efficacy as a proxy of past hydrological variability. Stalagmite $\delta^{18}O$ was found to be modulated by the frequency of recharge events and epikarst evaporation of storage water. Prolonged intervals between recharge events, such as droughts, resulted in higher stalagmite $\delta^{18}O$. Conversely, periods with more frequent recharge events and positive water balance, resulted in lower $\delta^{18}O$. Disequilibrium cave processes are likely to be enhanced during dry conditions, although it is argued that these will modulate $\delta^{18}O_{spel}$ in the same direction as epikarst evaporation, effectively amplifying the response of $\delta^{18}O_{spel}$ Extreme events, such as floods and droughts, were also captured in the stalagmite records, although potentially with a lag of several years. We verify that modern speleothems from semi-arid regions can be used to reconstruct hydroclimate due to variations in $\delta^{18}O_{spel}$ modulated by karst processes. Such records are archives of past changes in recharge rather than precipitation amount or surface temperature, as is commonly applied to speleothem records from non-water-limited regions.

1. Introduction

Drylands are water-limited regions where precipitation is less than potential evapotranspiration, causing either perennial or seasonal soil water deficits (D'Odorico and Porporato, 2006). They cover approximately 45 % of Earth's land surface and contain approximately 30% of its population (STAP, 2010). Globally, the largest expansion of drylands over the last 60 years has occurred in semi-arid regions (Huang et al., 2016). In Australia, a large portion of the area outside of the central arid desert regions are semi-arid and dry sub-humid drylands, which are also predicted to expand (Feng and Fu, 2013). Predicting the hydroclimatic response to climate change on the Australian continent, and particularly in SE Australia with the densest population, is therefore highly desirable.

One approach to understanding hydroclimate change is to use proxy records to obtain records of past hydroclimate variability. Speleothems are a particularly useful proxy in this regard, as they form directly from subsurface percolation waters (cave drips and seeps) which can contain geochemical indicators of environmental change (Fairchild and Baker, 2012). However, our current understanding of speleothem-forming processes is biased to cave-monitoring in regions with surplus water balances and frequent groundwater recharge. Significant exceptions are monitoring programs at Soreq Cave, Israel (Bar-Matthews et al., 1996; Ayalon et al., 1998; Even et al., 1986; Lange et al., 2003; Kaufman et al., 2003;); Sif Cave, Israel (Sheffer et al., 2011); Cathedral Cave, Australia (Cuthbert et al., 2014a, b; Rutlidge et al., 2014; Rau et al., 2015; Rutlidge et al., 2015; Markowska et al., 2016; McDonough et al., 2016; Baker et al., 2016a); and St. Michaels Cave, Gibraltar (Mattey et al., 2008; Mattey et al., 2010; Mattey et al., 2013; Baker et al., 2014). These studies have demonstrated that commonly used climate proxies in speleothems, such as $\delta^{18}O_{spel}$, may have different interpretations in dryland environments, owing to a higher likelihood of: (1)

discontinuous calcite precipitation, (2) non-equilibrium calcite precipitation, (3) high heterogeneity of karst hydrology, and (4) large soil moisture deficits which must be overcome to initiate recharge.

Drip interval and drip water supersaturation are theoretically the primary controls on kinetic fractionation during calcite precipitation, due to rapid degassing resulting in enhanced fractionation of the resulting $\delta^{13}C_{calcite}$ and $\delta^{18}O_{calcite}$ (Mühlinghaus et al., 2007, 2009). In dryland regions, the water-limited environment is a major control on drip hydrology and may consequently have the largest influence on in-cave isotopic fractionation. The dependence of $\delta^{18}O_{calcite}$ fractionation on drip interval is less than for $\delta^{13}C_{calcite}$, due to the buffering effects of the water solution (Mühlinghaus et al., 2009; Scholz et al., 2009). If degassing is sufficiently rapid, the CO_2 loss from solution is typically greater than the typical exchange time of several minutes between HCO_3^- and H_2O in solution (Scholz et al., 2009). This results in kinetic fractionation and higher $\delta^{13}C_{calcite}$ and $\delta^{18}O_{calcite}$ values (Mickler et al., 2006; Baker et al., 2011). In dryland caves with relatively low relative humidity, in-cave processes may also play a role in modifying the $\delta^{18}O$ in both drip waters and calcite. Deininger and Scholz (2019) demonstrated theoretically the significance of in-cave evaporation on driving disequilibrium isotopic fractionation for both $\delta^{18}O_{calcite}$ and $\delta^{13}C_{calcite}$ due to the loss of H_2O from the precipitating solution, which results in an increase in $Ca^{2+}_{(aq)}$ concentration, faster precipitation rates and greater isotopic fractionation.

Soil and karst hydrology can also be a significant control on the oxygen isotope signature observed in cave drips and associated speleothems in dryland regions. For example, drip water $\delta^{18}O_{drip}$ may be higher relative to precipitation $\delta^{18}O_{precip.}$ due to epikarst evaporation. In studies in Israel and Australia, this isotopic enrichment was observed to be +1.5 ‰ to +3 ‰,

92 respectively (Bar-Matthews et al., 1996; Cuthbert et al., 2014; Markowska et al., 2016). As in
93 more humid regions, hill-slope aspect can favour evaporative enrichment of subsurface water,
94 where slopes with greater sun exposure are associated with higher $\delta^{18}O_{drip}$ (Denniston et al.,
95 1999). The proportion of total precipitation likely to reach subsurface karst may be less in
96 drylands compared to humid regions, due to larger antecedent soil moisture deficits (Sheffer
97 et al., 2011; Jex et al., 2012). As a result, recharge $\delta^{18}O_{drip}$ may be biased towards high
98 magnitude precipitation events. For example, large convective storms are often associated
99 with lower $\delta^{18}O_{precip}$ values, even in mid-latitude regions (Ayalon et al. 1998; Fleitmann et
100 al., 2004; Treble et al., 2005). Rayleigh distillation, whereby $^{18}O/^{16}O$ isotopes are fractionated
101 between liquid and vapour, is enhanced in rapidly ascending air masses, resulting in
102 precipitation with low $\delta^{18}O$ values (Dansgaard, 1964; Rozanski et al., 1993). In a global
103 analysis of $\delta^{18}O_{drip}$ records, recharge-weighted $\delta^{18}O_{precip}$ was shown to best explain $\delta^{18}O_{drip}$ in
104 warm climate regions (Baker et al. 2019). Consequently, dryland speleothem $\delta^{18}O_{spel}$ should
105 be interpreted as a $\delta^{18}O_{precip}$ signal that is potentially highly modified by subsurface
106 evaporative enrichment and subject to larger recharge thresholds due to low antecedent soil
107 moisture and high evaporation rates. It may be more valid to consider these records as
108 reconstructions of recharge frequency/intensity rather than simply mean precipitation
109 $\delta^{18}O_{precip}$ (Markowska et al, 2016; Baker et al., 2019).
110
111 In dryland regions, $\delta^{18}O_{drip}$ is likely to be biased to the isotopic signature of recharge events,
112 and potentially also the extent of partial evaporation of epikarst water. In addition, cave
113 environments with low humidity and water supply limitations on drip rates lead to conditions
114 suitable for the disequilibrium precipitation of calcite are likely, resulting in greater extent of
115 $\delta^{18}O_{calcite}$ fractionation. Also, replication of coeval stalagmites oxygen isotope records may be
116 lower in dryland caves, which are more water-limited and sensitive to hydrological changes

at the individual drip level, compared to caves with well-mixed large water storage reservoirs from temperate environments. An assessment of the replicability of $\delta^{18}O_{spel}$ and hydroclimate signal contained in $\delta^{18}O_{spel}$ from a dryland site is required to increase our understanding of cave processes and investigate the dominant processes impacting the speleothem $\delta^{18}O$ record in water-limited environments. Here, we make such an assessment by comparing two modern, chronologically-constrained stalagmite $\delta^{18}O$ time series to the instrumental record. The instrumental era (<160 years) provides a critical test period for paleoclimate records derived from natural archives (Anderson et al., 1998; Mattey et al., 2008; Moquet et al., 2016). We use an established ^{14}C bomb-pulse age-model (Markowska et al. 2019) to constrain the chronology for the two modern (1935-2010 CE) speleothems from Cathedral Cave, SE Australia. A previously-developed karst hydrological model for the site (Cuthbert et al., 2014a) is extended for the period of speleothem deposition to model speleothem $\delta^{18}O_{spel}$. This model uses an evaporative enrichment function to assess whether the variability in $\delta^{18}O_{spel}$ can be explained by karst hydrology and the extent to which a climate signal is preserved in the stalagmite. The implications of these results for the identification of suitable speleothems for hydroclimate reconstruction in water-limited environments are addressed.

2. Background

2.1 Cave environment

Cathedral Cave is located at Wellington Caves Reserve, New South Wales, Australia (32° 37'S; 148° 56'E) (Figure 1, cave map: Figure S1). The cave descends to approximately 30 m below land surface and has formed within Devonian limestone which has been marmorised, leaving no primary porosity. Water flow is dominated by fracture-flow. A thin-layer of red-brown soil comprising clays, iron oxides, fine quartz sands, and calcite nodules,

with aeolian contributions, overlies the limestone (Baker et al., 2016a). Soil cover is not complete, with exposed karstified limestone abundant. Where present, soil thickness is typically less than 20 cm, with a thin (< 5 cm) organic layer followed by a sandy-clay textured soil down to bedrock (Berthelin et al. 2019). Cathedral Cave is within a temperate semi-arid region, with mean annual precipitation of 619 mm (1956-2005 CE) and pan evaporation of 1825 mm (1956-2005 CE) recorded 7 km north of the cave at Wellington (Bureau of Meteorology, 2015; climate data accessible at www.bom.gov.au/climate/data/). There is a large seasonal temperature variation, with monthly mean maximum ranging from 15 °C in July and 32 °C in January. Cathedral Cave is a long-term monitoring site for the modern monitoring of cave drip water hydrology in a water-limited environment. The stalagmites studied here come from South Passage, at approximately 25 m below land surface, and within the long-term drip water monitoring network (Jex et al 2012; Cuthbert et al 2014a).

Inactive speleothems are apparent throughout Cathedral Cave. Dripping is intermittent in the upper, drier chambers of the cave and speleothem formation is rare here, whilst speleothem formation dominates the deeper and wetter 'South Passage' where the stalagmites in this study were collected. South Passage generally has high relative humidity (97.1 ± 0.7%; Rau et al., 2015), little evidence of in-cave evaporative enrichment of water from evaporative pan experiments (<0.1 ‰ / h, $\delta^{18}O_{water}$) (Markowska et al., 2016), and high cave air CO_2 (mean concentration: 3535 ppm in winter, 7784 ppm in summer; McDonough et al., 2016). $\delta^{18}O_{drip}$ is dominated by evaporation of stored karst water under high humidity (Cuthbert et al., 2014a). During periods of low recharge, $\delta^{18}O_{drip}$ typically has more positive values (Cuthbert et al., 2014a; Markowska et al., 2016).

2.2 Wellington Caves climate, 1930 to 2010 CE

Figure 2 shows the temperature anomaly (°C), deep drainage (mm / d), monthly potential evaporation (mm) and annual rainfall amount (mm / a). At Wellington, mean annual temperature over 1900-2014 CE is 16.7 °C (Raupach et al. 2009, 2012; Figure 2). Overnight minimum temperature has increased by +0.4 °C since approximately 1950 CE (Figure 2), consistent with observations across the Australian continent in general (Fawcett et al., 2012; Trewin, 2013). The monthly Cumulative Rainfall Departure (CRD) and seasonal CRD, were calculated based on the cumulative departures from the mean monthly rainfall over the speleothem growth period 1930-2010 CE (Weber and Stewart, 2004; Bredenkamp, 1995). This approach is based on the principle that the cumulative departures from mean rainfall should broadly reflect changes in groundwater levels (eg. Butterworth et al., 1999). Monthly mean rainfall shows weak seasonality and large inter-annual variability (Markowska et al., 2016), associated with four major climate phenomena (El Niño Southern Oscillation (ENSO), Indian Ocean Dipole (IOD), Southern Annular Mode (SAM) and the Interdecadal Pacific Oscillation (IPO) (Pittock et al., 2006; Verdon-Kidd and Kiem, 2009; Ummenhofer et al., 2011; Christensen et al. 2013; King et al., 2013).

Climate predictions for SE Australia suggest further pressure on water resources, due to (1) anticipated decreases in cool season precipitation due to poleward expansion of the subtropical dry zone (Christensen et al., 2013) and decreasing groundwater recharge in (Crosbie et al., 2013), coupled with a global increase in drought frequency and/or severity (Dai, 2013). However, the general trend of declining rainfall over SE Australia during the latter half of the 20th Century reported by others (Nicholls, 2010; BoM, 2015) is not represented in annual rainfall totals at Wellington. Seasonal cumulative rainfall departure time-series exhibit contrasting seasonal trends, with increasing spring rainfall and decreasing

winter rainfall since 1960 CE. The latter has likely exacerbated the reduction in recharge, since infiltration of cool season rainfall tends to be more hydrologically effective due to lower potential evapotranspiration (PET) and higher soil moisture saturation. Two periods of deep drainage (defined as when water drains from the bottom of the modelled deep soil layer (6 m) into the groundwater stores) occur during the 1950's and early 1990's (Raupach et al., 2009, 2012; Figure 2).

Potential evaporation (PE) is derived using solar irradiance data from satellite imagery from 1990 to present, and for the period 1900-1990 is obtained by using the calibration against monthly climatological data for the post 1990 CE period. Mean and standard deviation PE is the same for both time periods (pre-1990: mean = 4.06 mm / day (3.94 - 4.18 95% CI, n=1080); post-1990: mean = 4.12 mm / day (3.88 to 4.37 95% CI, n = 290). A small decrease in PE variance (~5%, variance decreases from 4.4 to 4.2 mm / day) is observed in the time series prior to 1990 CE which is likely to be a calibration artefact. Most recently, the mid-2000's was correlated with years of persistently declining rainfall. This period, termed the "Millennium Drought" beginning in 1997 CE (Figure 2), experienced prolonged rainfall deficits brought about by widespread protracted dry conditions over most of continental Australia. The drought ended in 2010 CE, after ENSO activity switched to a strong La Niña phase. This brought about high precipitation resulting in large-scale flooding in many parts of southeast Australia and east Australia, including the town of Wellington in December 2010 CE (van Dijk et al., 2013). It was the second wettest December on record for the Murray-Darling Basin region, and Australia's wettest July to December period on record (NCC and BoM, 2011).

Drought conditions also occurred in the late 1940's (Figure 2), clearly seen in the sum of departures in mean monthly rainfall amounts (CRD; Figure 2). This "WWII Drought", which was widespread over eastern Australia during 1937 – 1945 CE (Ummenhofer et al., 2009), impacted summer and autumn rainfall totals most. This was followed by significantly wet conditions in the 1950's, including the highest annual rainfall on record and the largest flood on record delivering ~180 mm rainfall in 24 hours, flooding the local town of Wellington (~8 km from the study site) in 1955 CE. This coincided with a moderate La Niña, which had a strong effect across the eastern third of Australia (BoM, 2010).

2.3 Stalagmites WB and WC: morphology, chronology and drip regimes

The two stalagmites from Cathedral Cave, "WB" and "WC", were collected in mid-2010 CE from South Passage and were located approximately 5 m distance from each other. WB grew over a Bakelite (early plastic) cable installed in 1932 CE, the installation of which likely resulting in damage to the stalactite tip which re-invigorated dripping. Photographs of the sectioned samples are presented in Figure 3. WB and WC mostly consist of columnar calcite. The fabric of WB is more typically open columnar to microcrystalline types (Frisia, 2015), whereas WC is predominantly composed of compact columnar. In addition, WB appears to have been characterized by an initial overall greater porosity, which allowed destruction of the inter-crystalline porosity by early diagenetic cement precipitation (translucent calcite in Fig. 3A).

Carbonate $^{14}C_{spel}$ analysis results for stalagmites WB and WC were presented in Markowska et al (2019). Markowska et al. (2019) constructed an age model for each stalagmite which produced chronologies that cover the periods from 1936.7 ± 3.9 CE (WB) and 1982 ± 2.65

CE (WC) to the date of sampling. The resultant annual deposition rate is greater than 0.2 mm / year, and for WC over 0.7 mm / year, permitting high temporal resolution $\delta^{18}O_{spel}$ sampling (see section 3.1).

The median drip rate for seven other monitored drip sites in South Passage, where WB and WC were located, is slow, between 0 and 0.2 drips / min (Cuthbert et al., 2014a). The drip above the site of WC is also slow, with an average drip rate of 0.24 drips / min, slowing to 0 to 0.02 drips / min during non-recharge periods and up to 0.67 drips / min during recharge periods. No drip data was collected for WB due to insufficient drip height for drip logger installation; however, opportunistic observations suggest that WB had an overall faster drip rate than WC. In addition, during field observations in January 2016 CE the drip above WC was dry, but the drip above WBwas still active – suggesting that stalagmite WB had access to a larger karst water reservoir. Prior to January 2016 CE, the last rainfall event to significantly increase drip discharge in South Passage, and by inference increase the volume of water in the overlying stores, was in July 2013 CE (see Markowska et al 2016, Fig 2).

3 Methods

3.1 Carbonate $\delta^{18}O$ and $\delta^{13}C$ analysis

Slices 13 mm and 6 mm thick were cut from the central growth axis of stalagmites WB and WC respectively and then halved along the growth axis, on the right-hand side edge of an apparent dissolution hole in order to maximize sample recovery (Panel C, Figure 3). A Micromill 2000 ER-LR system with mechanical repeatability (precision) of 0.0127 mm was used to obtain sample powders. Carbonate powders were milled continuously from each stalagmite, using a 2 mm diameter tungsten carbide drill bit, along the edge of the growth axis in 0.1 mm increments (x-axis), 2 mm (y-axis) and 2 mm (z-axis) (WC, n = 220 and WB,

n = 360). Milling transects for isotopic analysis are shown in Figure 3, Panels C and D. Approximately 20-40 μg sub-samples of these powders were analysed on the MAT-253 Isotope Ratio Mass Spectrometer with Kiel carbonate device (Thermo Fisher Scientific, Bremen, Germany) at the Mark Wainwright Analytical Centre at UNSW Australia. They were reacted at 70 °C with 2 drops of 100 % phosphoric acid. The Kiel IV carbonate device settings used were a reaction one time of 420 s, a reaction two time of 120 s and a transfer time of 90 s. An integration time of 16 s and 8 cycles was used for the isotopic measurement of CO_2 gas. Data were standardized to the Vienna Peedee Belemnite (VPDB) scale using IAEA National Bureau Standards NBS-18 ($\delta^{18}O$ = -23.20 ‰ and $\delta^{13}C$ = -5.01 ‰) and NBS-19 ($\delta^{18}O$ = -2.20 ‰ and $\delta^{13}C$ = +1.95 ‰) using a two-point calibration. The analytical precision of the standards calculated for these datasets was 0.05 ‰ and 0.06 ‰, for $\delta^{13}C$ and $\delta^{18}O$, respectively.

3.2 Karst hydrology $\delta^{18}O$ model

$\delta^{18}O_{spel}$ is modelled using a Soil Moisture Balance (SMB) model first presented in Cuthbert et al. (2013), coupled with a karst hydrology model (Cuthbert et al., 2014a) to simulate groundwater recharge, shallow karst flow, and oxygen isotopic composition of drip waters. The combined SMB-karst model was parameterised for Cathedral Cave and successfully used to model drip water isotopic composition for a range of drips from South Passage for monthly-integrated samples (Markowska et al., 2016) over a two-year period in Cuthbert et al. (2014a). Unique to the study of Cuthbert et al (2014a) was a function to model the isotopic evolution of drip waters due to epikarst evaporation under high humidity conditions following Gonfiantini (1986). This accounted for the measured ^{18}O enrichment of karst drip waters relative to rainfall ^{18}O, which fell on the local meteoric waterline rather than an

289 evaporation line typical of water evaporated under low humidity (Cuthbert et al., 2014a). The
290 sensitivity of all model parameters was assessed in Cuthbert et a (2014a). The model
291 structure (Figure S2) and code are available in the Supplemental Materials.
292
293 Here, the model is extended back through the 20th century, keeping the same parameters as
294 previously calibrated for the SMB-karst model. For the isotope model, since the previous
295 calibration was carried out for a wide range of drips, a slight modification was needed for the
296 parameters to best represent the drip feeding WB. Based on field observations (see section 2),
297 WB had a relatively faster drip rate compared with the range of drips previously represented
298 in the model. It was assumed from this higher drip rate, that WB is fed by a larger store.
299 Hence, the parameter S2Lim (the depth in the modelled box karst reservoir where epikarst
300 evaporation 'turns on') was decreased from 60 mm to 20 mm, to reduce the level at which
301 evaporation became important. In the parameterisation of this model, perhaps
302 counterintuitively, a higher S2Lim parameter (greater depth) results in higher evaporation
303 due to the greater range of depths where the evaporation term is 'turned on', 0-60 mm
304 opposed to 0-20 mm. The epikarst evaporation rate was also reduced from 0.04 mm / d to
305 0.01 mm / d in order to capture an oxygen isotopic composition closer to mean rainfall.
306
307 Precipitation-weighted mean annual rainfall ($\delta^{18}O_{precip}$ = ~-4 ‰) was used as the model input,
308 based on two years of rainfall monitoring (Cuthbert et al., 2014a). This value is close to
309 modern groundwater values (mean = -4.78 ‰, n = 11) from Spicers Creek catchment 68 km
310 away (Morgan et al., 2006) and at in two boreholes at Wellington Caves that were monthly
311 sampled between November 2013 and July 2014 (BH1: -4.28 ± 0.29‰; BHGolf: -4.70 ±
312 0.20‰; Keshavarzi, 2018). Monthly-integrated $\delta^{18}O_{precip}$ presented in Cuthbert et al. (2014)
313 over the two-year monitoring period has a very weak relationship with rainfall amount (r^2 =

0.03; $p > 0.05$ n = 24). However, end member event isotopic rainfall composition of < 5 mm and > 45 mm suggests there may be a stronger relationship if event-based samples are considered (Figure 4, Supplementary Figure 2). Opportunistic rainfall event samples (0.5 - 24 h), sporadically collected over 2010 - 2012 CE (data available as Supplemental Materials). Samples were stored in glass bottles with no headspace and analysed on the Los Gatos © cavity ring down mass spectrometer at UNSW Australia. The overall precision was ± 0.12 ‰ $\delta^{18}O$ and ±1.2 ‰ δD. Event end-member samples showed a moderate $\delta^{18}O_{precip}$ relationship with daily rainfall amount ($r^2 = 0.48$; $p < 0.05$, n = 12) (Figure S3). This correlation was considered too weak to be used as a transfer function to enable a calculated rainfall $\delta^{18}O_{precip}$ time series to be used as the model input. However, as a test of how the model might perform if such an input was known, a value of $\delta^{18}O_{precip} = -12$ ‰ was used as the input value for the most extreme rainfall events (>120 mm / d) observed at this site based on event rainfall samples (e.g. $\delta^{18}O_{precip.} = -11.3$ ‰ after ~105 mm rainfall over two days). All other parameterisation was the same as in Cuthbert et al. (2014a).

Since the original model was calibrated for drip water oxygen isotopes, a correction was required to convert the modelled data ($\delta^{18}O_{drip}$ VSMOW) to a calcite equivalent ($\delta^{18}O_{calcite}$ VPDB) for comparison with the measured $\delta^{18}O_{spel}$. This conversion was based on a CO_2-H_2O fractionation factor of 1.0412, an acid fractionation factor for H_3PO_4 liberated CO_2 from calcite of 1.01025 (Freidman and O'Neil, 1977), and a H_3PO_4-liberated CO_2 from VPDB-CO_2 in equilibrium with VSMOW of 1.00027 (Gonfiantini, 1984; Hut, 1987) following Coplen (1988), Eq. 12, (p. 295). The in-cave temperature dependent fractionation at the time of calcite precipitation from drip water was calculated from the equation of Kim and O'Neil (1997) and the mean annual surface temperatures from the AWAP database (Raupach et al., 2009, 2012) to produce predicted calcite $\delta^{18}O_{calcite}$. It is assumed that evaporative cooling is

negligible at the stalagmite sites of WB and WC in South Passage, as the RH is ~97% most of the time (Rau et al., 2015)

4 Results

4.1 Stalagmite $\delta^{18}O$ time series

Time series and $\delta^{18}O_{spel}$ vs. $\delta^{13}C_{spel.}$ scatterplots for stalagmites WB and WC are compared in Figure 5. The isotopic time series for WB is seasonally resolved (~4.9 samples / year) and for WC is bi-monthly resolved (~7.9 samples / year). The isotopic mean of WC is offset overall by approximately +0.5 ‰ ($\delta^{18}O_{spel}$) and +1.2 ‰ ($\delta^{13}C_{spel}$) relative to WB (Figure 5), and by +0.3 ‰ ($\delta^{18}O_{spel}$) and +1.4 ‰ ($\delta^{13}C_{spel}$) over the period of overlapping growth. Both stalagmites have $\delta^{18}O_{spel}$ approximately 1 ‰, higher than the precipitation-weighted mean annual rainfall when rainfall is considered on the equivalent (VPDB) scale, i.e. mean rainfall of -4 ‰ VSMOW should theoretically form calcite with $\delta^{18}O$ of -4.9 ‰ using the equation from Kim and O'Neil (1997).

The two stalagmite records overlap from 1982 ± 2.65 CE onwards. With respect to mean $\delta^{18}O_{spel}$, the comparison between the two stalagmite records between 1990 and 2004 CE is typically within 0.5 ‰ (Figure 6). Both $\delta^{18}O$ records show sub-decadal and longer-term trends throughout their respective growth periods, but there is typically less variability in WB which appears more smoothed relative to WC (Figure 5).

Comparing the sub-decadal trends and peaks, between 1982 and 1990 CE, there is little agreement between stalagmites, with $\delta^{18}O_{spel}$ maxima in 1985 and 1987 CE in WC not represented in WB. Starting in 1990 CE, $\delta^{18}O_{spel.}$ becomes more positive in both stalagmites

by ~1 ‰ for about 5 years, followed by a ~1 ‰ decrease until 2000 CE. Following this, $\delta^{18}O_{spel}$ of both stalagmites begins to increase again by ~1.2 ‰, with maximum values around 2002 and 2003 CE (Figure 5). The subsequent decrease in $\delta^{18}O_{spel}$ was greatest in WB (1 ‰) compared to WC (0.4 ‰). After this minima, $\delta^{18}O_{spel.}$ for both stalagmites increased by +1.4 ‰ up to 2010 CE. This was a smooth $\delta^{18}O_{spel.}$ increase in WB, whereas in WC the general increasing trend was punctuated by peaks and troughs in $\delta^{18}O_{spel.}$ every 1 - 2 years (Figure 5). We statistically compared the correlation between the two stalagmites for the post 1990 CE period, after interpolating the $\delta^{18}O_{spel}$ series to a common timescale, normalising to z values, and detrending (0.05 z-score /yr), and then investigated all correlations within the chronological uncertainties of the two stalagmites. Despite the visual correlations, the maximum Kendall's Tau value was 0.21, confirming differences in the number, and amplitude of, isotope peaks and troughs between the stalagmites.

Considering the long-term WB $\delta^{18}O_{spel}$ record, $\delta^{18}O_{spel}$ begins at -5.4 ‰ in 1936 CE and increases to -3.3 ‰ by 1948 CE, punctuated by a short-term trough in 1947 CE (Figure 5). WB $\delta^{18}O_{spel.}$ decreases to -5.0 ‰ at 1950 CE. A further increase and decrease of ~1 ‰ occurs, before an increase to -2.5 ‰, the highest value in the WB time series, in 1953 CE. The lowest value in the record (-6.4 ‰) occurs shortly after (1956 CE), a 4 ‰ decline in three years. This is accompanied by a slower growth rate (0.12 mm / a) continuing until 1965 CE, where WB $\delta^{18}O_{spel}$ increases to -3.1 ‰ in 1966 CE, although values are ~1 ‰ lower in the early 1960's. $\delta^{18}O_{spel}$ decreases by ~1 ‰ again until 1970 CE, after which it remains stable at the long-term $\delta^{18}O_{spel}$ isotopic mean of -4.1 ‰ until the early 1980's.

4.1.1 Stalagmite $\delta^{18}O$ vs $\delta^{13}C$

387 The $\delta^{18}O$ vs $\delta^{13}C$ relationship for WC is strong as shown in the scatterplot inset in Figure 5
388 ($r^2 = 0.77$), suggesting that WC may have precipitated under enhanced disequilibrium
389 conditions (Desmarchelier et al., 2000). Conversely, WB shows no relationship between $\delta^{18}O$
390 and $\delta^{13}C$ ($r^2 = 0.00$), as judged by the scatterplot in Figure 5. This agrees with the observed
391 speleothem fabrics where WB is more typically open columnar to microcrystalline types,
392 whereas WC is predominantly composed of compact columnar. Frisia et al. (2018) propose
393 that cave calcite grows by nanocrystal aggregation rather than classical mechanisms; compact
394 crystals aggregate and then coalesce, whereas more porous, nanocrystals are bridged by
395 organics. The compact columnar calcite of WC is due to the slow drip rate, with drip water
396 having time to degas on the speleothem surface, and with calcite precipitated without much
397 disturbance by colloidal and particulate matter. In contrast, WB has more open and
398 microcrystalline fabrics, which can be indicative of the presence of dissolved organic matter
399 and more disturbance by colloidal and particulate matter. These are representative of a
400 quicker hydrological connectivity to the surface, agree with the observation of a faster drip
401 rate, and less disequilibrium calcite deposition from the film of fluid (Dreybrodt and Scholz,
402 2011; Deininger et al 2012).
403

404 ### *4.1.2 $\delta^{18}O$ relationship with the instrumental climate record*

405 Figure 6 shows the two $\delta^{18}O_{spel}$ records (Panel E) alongside variables: deep drainage (mm / d;
406 Panel E), water excess (mm / d; Panel D), annual CRD, winter CRD, PE (mm / d; Panel C),
407 Southern Oscillation Index (SOI; Panel B) anomalies and IOD events (Panel A). $\delta^{18}O_{spel.}$
408 trends are broadly anti-correlated to the monthly CRD (Figure 6). For example, a long-term
409 15-year decline in the CRD over 1935-1950 CE, an indicator of groundwater levels, is
410 mirrored by an overall increase in $\delta^{18}O_{spel}$ .Water balance deficits (P < ET) also occurred in

411 12 of the 15 years (Figure 6) and the period 1937-1945 CE was recognised as a drought due
412 to high water deficits (WWII Drought; Figure 6). WC $\delta^{18}O_{spel}$ values are also higher during
413 drought periods (i.e. Millennium Drought; Figure 6) and show a continuous positive trend,
414 for example from -4.1 ‰ in 1999 CE to -2.4 ‰ in 2008 CE (Figure 6). In addition, during the
415 same period, six periodic oscillations in WC $\delta^{18}O_{spel.}$ were observed, approximately 1 ‰ in
416 amplitude and approximately 1 - 2 years in wavelength (numbered 1 to 6; Figure 6). These
417 correspond with the longest (six consecutive years) period of annual water deficit (P<ET)
418 (numbered 1 to 6; Figure 6). The oscillations in the stalagmite do not all occur synchronously
419 with the climate record, but are within chronological error ± 2.65 years. This asynchrony
420 could be due to the uncertainty in the chronology because of non-linear growth or a non-
421 linear transfer function of surface hydroclimate dynamics to the stalagmite. WB $\delta^{18}O_{spel}$
422 values in the Millennium Drought were also higher but not dissimilar from other dry (but not
423 drought) periods in the time series (e.g. 1995-1996 CE) although $\delta^{18}O_{spel}$ did persist above
424 the arithmetic mean for most of the 2000's (Figure 5).
425
426 Conversely, during periods of water excess (P > ET), lower $\delta^{18}O_{spel}$ is typically observed
427 (Figure 6). For example, in 1950 CE Wellington experienced the highest rainfall year on
428 record (1386 mm / a), resulting in an estimated deep drainage of ~0.45 mm / d (deep drainage
429 from AWAP data; Figure 6) and water excess (P - ET from AWAP data; Figure 6),
430 coinciding with a trough in $\delta^{18}O_{spel}$. During periods of high and sustained water excess, e.g.
431 1969-1974 CE (Figure 6), $\delta^{18}O_{spel}$ is less variable and is similar to arithmetic mean $\delta^{18}O_{spel}$
432 values (Figure 5).
433
434 A major flood event (1955 CE) is the only part of the WB $\delta^{18}O$ time series outside of the
435 range of observed drip $\delta^{18}O_{water}$ (e.g. -6.4 ‰ VPDB; Figure 5). In the historical record,

436 flooding occurred in the town of Wellington in February 1955 CE due to a trough bringing in
437 moist airflow associated with a monsoon depression moving down from Queensland
438 (Australian Bureau of Statistics, 2008), delivering 178 mm of rainfall in 24 hours and ~240
439 mm over a four-day period. The resulting February 1955 CE rainfall was the highest on
440 record (BoM, 2010). This flooded the Wellington township and surrounding regional areas
441 bringing unprecedented rainfall to an area which, in decades previous, had been in drought
442 conditions (Thorpe and Tweedie, 1956; Walker, 2010). Rainfall event samples over 2011-13
443 CE (Figure 5) at Wellington revealed that modern $\delta^{18}O_{precip}$ of extreme rainfall events are
444 likely to be isotopically depleted (e.g. -11.4 ‰ VSMOW, ~105 mm rainfall). The flood
445 period is a clear outlier in $\delta^{18}O_{spel}$, with rapid depletion starting in 1955 CE and continuing to
446 1957 CE (Figure 6). The timing of the surface flood event and rapid $\delta^{18}O_{spel}$ change occur
447 almost synchronously (Figure 6), suggesting that the karst hydrological response to these
448 types of events has no measurable lag, although their persistence in the $\delta^{18}O$ record continues
449 years after the flood occurred (e.g. 1956-57 CE) demonstrating the vadose zone hydrologic
450 memory.
451

452 # 5 Discussion

453 ## 5.1 Climatic controls on stalagmite $\delta^{18}O$

454 The frequency of effective recharge and partial evaporation of water stored in the karst
455 control the drip $\delta^{18}O_{drip}$ variability at Cathedral Cave (Cuthbert et al., 2014a; Markowska et
456 al., 2016). Drip water monitoring has demonstrated that the process of epikarst evaporation
457 drives the isotopic composition of storage water towards higher values during dry periods.
458 When recharge occurs, this dilutes the high ^{18}O storage water with low ^{18}O from rainfall
459 events that generate recharge (Cuthbert et al 2014a). With no seasonality in precipitation at

460 the site, annual cycles of depletion and enrichment in $^{18}O_{drip}$ of sampled drips have not been
461 observed. Furthermore, there is no correction between monthly rainfall amount and monthly
462 $\delta^{18}O_{drip}$ composition (Markowska et al., 2016).
463
464 The irregular timing of recharge events explains an absence of regular, annual $\delta^{18}O_{spel}$ cycles
465 in the stalagmite time series (Figure 5). The irregular timing of recharge events means that
466 variability in $\delta^{18}O_{spel}$ due to intra-annual changes in $\delta^{18}O_{precip}$ will not be uniform (i.e. varying
467 on a seasonal basis) and are more likely synoptically driven depending on moisture source of
468 individual rainfall events. Monthly $\delta^{18}O_{drip}$ data suggest that epikarst evaporation could be
469 responsible for the magnitude of the high frequency increases in $\delta^{18}O_{spel}$, with shifts in
470 $\delta^{18}O_{drip}$ of up to ~2 ‰ in the space of several months (Cuthbert et al 2014a). Over the 3-year
471 drip water monitoring period (2010-2013 CE) drip waters in South Passage varied by 2.8 *‰*
472 (n = 85) with a standard deviation of 0.45 *‰* (Cuthbert et al 2014a). Observed $\delta^{18}O_{spel.}$
473 variability is all within the same range of observed $\delta^{18}O_{drip}$ (once converted to the equivalent
474 VPDB scale using the temperature dependent fractionation equations of Kim and O'Neill
475 (1997)). One exception is the 1955 CE flood period discussed in section 4.2.3. With limited
476 recharge, $\delta^{18}O_{spel}$ increases from -5.0 ‰ to -4.2 ‰ (Figure 6) over the WWII drought in
477 1937-1945 CE. Conversely, recharge causes $\delta^{18}O_{spel}$ to move towards lower values. For
478 example, $\delta^{18}O_{spel}$ shifted from -3.3 ‰ in previously dry years to -4.9 ‰, a difference of
479 ~1.5 ‰, after very high precipitation amount in 1950 CE (Figure 6). Overall, $\delta^{18}O_{spel}$ data
480 supports the previous conclusions in Cuthbert et al. (2014a) from drip monitoring studies in
481 Cathedral Cave where epikarst evaporation isotopically enriches storage water during dry
482 periods, punctuated by recharge during wet periods which dilutes high ^{18}O storage water with
483 low ^{18}O water from recharge.
484

5.2 Mechanisms affecting speleothem $\delta^{18}O$ composition

5.2.1 Cave climate

High humidity at the end of the South Passage chamber >97 % (Rau et al., 2015) means both stalagmites would have experienced a similar cave air environment. Limited ventilation occurs, with the absence of noticeable airflow, with a measurable decrease in CO_2 from an average of 7784 ppm in summer to 3535 ppm in winter (McDonough et al., 2016). As both stalagmites are at least seasonally resolved, one would expect to see any seasonal changes in $\delta^{18}O_{spel}$ driven by cave ventilation effects, particularly in stalagmite WC with bi-monthly resolution. Seasonally driven ventilation effects are likely to lead to higher $\delta^{18}O_{spel}$ and $\delta^{13}C_{spel}$ due to changing the relative pCO_2 and determining the rate of degassing CO_2 from a thin film of water (Baker et al., 2011; Deininger et al., 2012; Scholz et al., 2012). Annual trends in isotopic composition have been observed in speleothems in well-ventilated caves (Mattey et al 2008). However, there is no annual periodicity in $\delta^{18}O_{spel}$ or $\delta^{13}C_{spel}$ in stalagmites WC and WB and ventilation is therefore an unlikely cause for the higher $\delta^{18}O_{spel}$ observed here. Instead, it is likely that the interplay of supersaturation and drip rate are the dominant controls on growth rate and disequilibrium fractionation.

5.2.2 Kinetic isotope fractionation effects during precipitation

Cave parameters other than relative humidity and wind velocity may also cause $\delta^{18}O_{spel}$ to deviate from isotope equilibrium precipitation e.g. temperature, drip interval, drip water supersaturation with respect to calcite (Day and Hendersen (2011), Dreybrodt and Scholz (2011) and Deininger et al. (2012)). The estimated theoretical equilibrium of precipitation at Cathedral Cave using the measured precipitation-weighted mean annual rainfall is -4.89 ‰ VPDB ($\delta^{18}O_{precip}$). This is calculated using the equation of Kim and O'Neil (1997), which does not account for in-cave processes in its formulation. The majority of $\delta^{18}O_{spel}$ values for

stalagmite WB and all $\delta^{18}O_{spel}$ values for stalagmite WC are greater than the predicted equilibrium value, with relative overall offsets of 0.8 ‰ and 1.3 ‰, respectively. This suggests that stalagmite $\delta^{18}O_{spel}$ rarely if ever reflects the mean isotopic composition of precipitation at Cathedral Cave. Furthermore, the overall relationship between $\delta^{18}O_{spel}$ and $\delta^{13}C_{spel}$, an indicator for disequilibrium processes (Dreybrodt and Scholz, 2011), over the whole time series for stalagmite WC is strong ($r^2 = 0.77$) and likely precipitates under greater disequilibrium conditions (Figure 5). WB shows no relationship ($r^2 = 0.00$) and likely precipitates closer to equilibrium conditions (Figure 5).

High drip water pCO_2 can cause $\delta^{18}O_{spel}$ to deviate from isotope equilibrium due to kinetic isotope fractionation during calcite precipitation. Evidence for this at Cathedral Cave includes the fast growth rates for WB and WC (~ 0.53 and ~0.76 mm / a, respectively). Calcium concentration is one of the driving forces behind growth rate (Baker et al., 1998; Dreybrodt, 1999; Baker et al., 2016b) and high mean drip Ca concentration ~2.2 mmol / L^{-1} (Baker et al., 2016b) is also observed. Changes in drip water pCO_2 can occur over time, which in turn could control the amount of kinetic isotope fractionation and changes in $\delta^{18}O_{spel}$ over time. Prior calcite precipitation (PCP), vegetation cover, fire, and vadose zone microbial and root respiration (Baker et al., 2016b) can all control the degree of host rock dissolution and potentially the extent of drip water pCO_2. At Wellington, fire has not been experienced at the site and thus can be ruled out as an important process. Trees present over the cave are potentially providing an additional source of vadose zone CO_2 at Cathedral Cave, and their regrowth over several decades could lead to long-term changes in drip water pCO_2 and $\delta^{18}O_{spel}$ over time through changes in the amount of root respiration. Field observations reveal the stagnant chamber adjacent to South Passage has consistently high CO_2 (up to ~50,000 ppm), and deep tap roots from large eucalyptus trees growing on the surface (e.g.

above WC; Figure 3; Panel K) are clearly visible in neighbouring Gaden Cave. Over shorter time periods, variations in PCP could be an important control drip water pCO_2 and associated kinetic isotope fractionation during calcite precipitation. With intermittent recharge at the site, there is adequate time for PCP to occur in the karst stores supplying drip water to WB and WC, and in drier conditions, Ca remaining in solution in the drip water is hypothesised to decrease due to PCP. The extent of PCP at the site is currently poorly constrained.

Drip interval is also important in kinetic fractionation as it determines the replenishment rate of solution on top of the stalagmite, and the isotope fractionation potential is a time dependent process controlled by the solution residence time (Mühlinghaus et al., 2007, 2009; Hartmann and Baker, 2017). Longer drip intervals may have a significant effect on enriching ^{18}O and ^{13}C due to Rayleigh distillation processes (Mickler et al., 2006; Mühlinghaus et al., 2009). Specifically, it is the increasing enrichment in the HCO_3^- reservoir resulting from degassing and subsequent $CaCO_3$ precipitation (Mickler et al., 2006). Mickler et al. (2006) observed progressive increases in $\delta^{18}O$ away from the growth axis, as high as +1.7 ‰. Day and Henderson (2011) estimated ~+1.5 ‰ enrichments in ^{18}O induced from the combination of both rapid DIC depletion and evaporation. For very slow drip rates (~1 drip / 50 min) isotopic exchange with the cave atmosphere is also important and will cause the upper layers of solution to be in equilibrium with cave atmosphere (Scholz et al., 2009; Dreybrodt et al., 2011). However, this is less likely to be important here as the average drip rate in South Passage is between 0 and 0.2 drips / min (Cuthbert et al., 2014a) and is usually > 1 drip / 15 min.

A conceptual model for dryland caves using Cathedral Cave and stalagmites WC and WB as an example is shown in Figure 7. The effects of both in-cave disequilibrium processes and

560 epikarst evaporation shift $\delta^{18}O_{spel}$ in the same direction; towards higher values with respect to
561 precipitation-weighted mean annual rainfall. Both processes will be enhanced during drier
562 phases. Disequilibrium fractionation can provide one explanation for the positive offset of
563 WC $\delta^{18}O_{spel}$ relative to WB, as well as the contrasting $\delta^{18}O$ vs. $\delta^{13}C$ relationship, as WC is
564 hydrologically fed by a different store which is likely a smaller overflow, evidenced by its
565 slower drip rate and the fact that it stops dripping in drier periods. This may be due to its
566 position directly beneath a large eucalyptus tree (Figure 3, Panel K) where roots have
567 penetrated to access the water store. Although not visible in this cave, there are roots clearly
568 visible at a similar depth in neighbouring Gaden Cave and similar observations have been
569 made in Golgotha Cave, SW Western Australia (Treble et al., 2016). Disequilibrium alone
570 cannot account for the magnitude of variability >2 ‰ in $\delta^{18}O_{spel}$, suggesting that the
571 influence of epikarst evaporation observed in drip waters (Cuthbert et al., 2014a; Markowska
572 et al., 2016) is also important for the stalagmite $\delta^{18}O_{spel}$ variability.
573
574 ***5.2.3 Climate signals in $\delta^{18}O$***
575 Two significant hydrological drought periods occurred over the stalagmite growth period; the
576 "Millennium Drought" (1997-2010 CE) and the "WWII Drought" (1937-1945 CE). The
577 Millennium Drought was characterized by increases in PE, warmer temperatures, water
578 deficits (decreasing P-ET), an unusually long succession of positive IOD phases (Figure 6;
579 Ummenhofer et al., (2011)) and a decrease in the rainfall intensity, rather than the number of
580 rain days (Verdon-Kidd and Kiem, 2009). However, it is suggested that the WWII Drought
581 (1937-1945 CE) was more severe in intensity than the Millennium Drought (Jonathan et al.,
582 2015). It was also a precursor to the largest rainfall deficit period (1947-49 CE) during the
583 WB stalagmite growth period and was characterised by a persistent 10-year decline in CRD
584 (Figure 6). Whilst both droughts exhibit negative P-ET, suggesting rainfall deficits, the

585 Millennium Drought, in terms of P-ET, appears to be drier. In contrast, the WWII Drought
586 was characterised by a persistent 10-year decline in CRD (Figure 6) and the greatest negative
587 cumulative departures from mean rainfall, suggesting depleted groundwater reservoirs. This
588 is in direct contrast to the Millennium Drought, which had a slightly positive CRD,
589 suggesting groundwater reservoirs were less negatively impacted, despite drought conditions.
590
591 The fabric of stalagmite WB during the decline in CRD over 1937 to 1947 CE contains
592 microsparite layers (Figure 3; Panels E, I, J). Microsparite forms via episodes of nucleation
593 via nanocrystal aggregates, often involving biomediation, which occurs during slow to no
594 drip periods or during prolonged dry phases (Frisia, 2015). This supports the evidence that
595 the karst aquifer feeding WB was likely declining in response to this drought period.
596 However, $\delta^{18}O_{spel}$ over the drought period was not significantly higher compared to the
597 arithmetic mean (WB, Figure 6). Positive trends accelerated several years later, for example
598 in 1948 CE when $\delta^{18}O_{spel}$ reached -3.3 ‰, coinciding with the highest negative rainfall
599 departures (low CRD, Figure 6). Similarly, after significant rainfall during the 1950's, which
600 led to increased deep drainage, $\delta^{18}O_{spel}$ fluctuated by 1-2 ‰, but continued an upward trend
601 to a maximum of -2.5 ‰ in 1954 CE (WB, Figure 6), before the recharge response occurs.
602 These responses suggest that there is a lag between surface rainfall and karst store recharge,
603 where low karst store volumes persist even after surface drought conditions had abated, thus
604 allowing them to be more susceptible to epikarst evaporation and subsequent $^{18}O_{water}$
605 enrichment. This may imply that a large reservoir is feeding stalagmite WB, which became
606 depleted in volume over the drought period, and took a long time to be refilled. As a result,
607 when the karst reservoir was in this low volume phase, the stored water may be more
608 sensitive to karst evaporative enrichment due to larger air-filled voids and conditions suitable
609 for PCP, shown in Figure 7. Consequently, stalagmite $\delta^{18}O_{spel}$ correlations to dry surface

610 climate conditions are drawn out due to an apparent persistence or memory effect of previous
611 conditions or due to non-linear responses to changes in climate. The stalagmite record
612 suggests that it took a decade after the drought abated (1945 CE) for karst store volumes to
613 significantly increase, because although there is evidence of recharge from high rainfalls in
614 the 1950's (Figure 6), the $\delta^{18}O_{spel}$ trend continues to rise, and fabric contains microsparite
615 layers until the 1955 CE flood. The effect of this drought on long-term store levels might
616 have been more impactful than the Millennium Drought, although there is no data from years
617 after the Millennium Drought as the stalagmite was removed from the cave in 2010 CE.
618 However, stalagmite fabric precipitated during the Millennium Drought contained no
619 microsparite layers, perhaps suggesting that its impact on the shallow karst water reservoir
620 was not as extreme.
621
622 ***5.2.4 Karst $\delta^{18}O$ modelling***
623 A combined SMB-karst model was employed to determine whether $\delta^{18}O_{spel}$ can be modelled,
624 using epikarst evaporation of water as the major driver dominating trends in $\delta^{18}O_{spel}$ by
625 raising $\delta^{18}O_{drip}$. The parameterisation of the karst model has been optimised in Cuthbert et al.,
626 (2014a) for this field site. The model results are shown in Figure 8 and a model schematic is
627 shown in Supplemental Material in Figure S2. Comparing first the model output for
628 stalagmite WC, $\delta^{18}O_{modelled}$ is generally in good agreement with $\delta^{18}O_{spel}$. Almost all major
629 peaks and troughs could be replicated within the age uncertainty (± 2.65 years) suggesting
630 that epikarst evaporation provides a good explanation for the variability in WC $\delta^{18}O_{spel}$. One
631 peak in $\delta^{18}O_{spel}$ in 2001 CE was not captured in $\delta^{18}O_{modelled}$ but all five subsequent peaks were
632 within ± 1 years of $\delta^{18}O_{spel}$. There is an offset of ~0.5 - 1 ‰ between WC $\delta^{18}O_{modelled}$ and
633 $\delta^{18}O_{spel}$ values (e.g. 1990 CE). This may be because the model only considered karst
634 evaporation and temperature dependent fractionation (Kim and O'Neil, 1997) as the two main

drivers of $\delta^{18}O_{spel}$ variability, and not potential additional kinetic effects. The co-variation of WC $\delta^{18}O_{modelled}$ and $\delta^{18}O_{spel}$ values here strongly suggest that WC can be explained by a simple single-reservoir model, which is very sensitive to karst evaporation and changes in water storage volumes, controlled by alternating periods of recharge and decline.

Conversely, WB $\delta^{18}O_{modelled}$ and $\delta^{18}O_{spel}$ values are less in agreement (Figure 8). The first peak in $\delta^{18}O_{modelled}$ does not appear in $\delta^{18}O_{spel}$, although it coincides with the stalagmite growth nucleation phase. Otherwise, the first part of the WB $\delta^{18}O_{modelled}$ time series is generally in good agreement with $\delta^{18}O_{spel}$ until ~1950 CE. As expected, given the prescribed depleted isotopic input for large rainfall events, the 1955 CE flood is captured with similar magnitude to the observed $\delta^{18}O_{spel}$. The long stable period from 1970-1990 CE also shows good agreement with WB $\delta^{18}O_{modelled}$ and $\delta^{18}O_{spel}$, although $\delta^{18}O_{modelled}$ is offset in some parts by up to 0.5 ‰. The Millennium Drought, which is captured as a rising trend punctuated by toughs and peaks in $\delta^{18}O_{modelled}$ for WC, is not well represented by the model for WB. Complex flow behaviour, variable lags and have been demonstrated in this cave system (Markowska et al., 2016). This suggests that WB cannot be explained by a simple single-reservoir model and likely is fed by multiple reservoirs. WB's position in the cave, behind a large flowstone feature, which has grown over the entire Quaternary period, suggests a possible connection to a larger storage reservoir. Thus, while the model used can provide insights into the likely processes controlling $\delta^{18}O_{spel}$, it also likely points to the necessity of (1) a more complex multi-store model to capture the variability in WB, (2) quantification of disequilibrium processes from additional cave monitoring of drips feeding WB and WC, and (3) a longer time series of drip water isotope data for model calibration before the model can reliably hindcast past droughts and recharge events.

The selection of speleothems for analysis is subject to trade-offs due to the sensitivity of $\delta^{18}O_{spel}$ to epikarst evaporation and volume and discontinuous growth, where smaller near-surface reservoirs with large headspaces will show the greatest epikarst evaporation sensitivity but also may be more likely to exhibit discontinuous growth by virtue of their small storage volumes. Figure 9 shows the relationship between the modelled offset in $\delta^{18}O$ from the mean rainfall composition due to epikarst evaporation, the water storage depth where epikarst evaporation 'switches on' (S2lim) and the epikarst evaporation rate (mm/d). The location of the two stalagmites from this study are shown in this parameter space (Figure 9). For a water-limited environment as modelled here, the amount of epikarst evaporation is a small fraction of the total karst water balance, and the continuity of speleothem growth can be assumed to be solely a function of the storage volume via S2lim. Assuming that our 1D model store approximates to the actual 3-dimensional karst void, then the more sensitive a stalagmite is to evaporation the more likely it is to have discontinuous growth or longer hiatuses. At Wellington Caves, the near vertical bedding combined with hypogene solution features means that the development of vertical voids is a reasonable conceptualisation. Figure 9 shows that WC $\delta^{18}O$ will be more affected by karst evaporation processes compared to WB. Therefore, WC is more sensitive to climatic influences including changes in water balance. Similarly, climatically sensitive samples, potentially identified through fabric analysis, could therefore be more useful for paleoclimate applications.

6. Conclusion

This study reveals that the use of $\delta^{18}O_{spel}$ as a source of paleoenvironmental information does not require the prerequisite that speleothems formed under isotopic equilibrium conditions. However, coeval stalagmites oxygen isotope records have differences that we relate to their individual hydrology and flow path, demonstrating that in a water-limited environment,

685 $\delta^{18}O_{spel}$ can be sensitive to hydrological changes at the individual drip level. Because of this,
686 replication of coeval stalagmites oxygen isotope records may be lower in dryland caves
687 compared to caves with well-mixed large water storage reservoirs from temperate
688 environments. This is conceptually demonstrated in Figure 7, by showing the relative sizes of
689 water stores feeding drips WC and WB during dry conditions. In Figure 7 the overflow store
690 feeding WC, is quickly depleted in dry conditions as opposed to WB, which is connected to a
691 more consistent water source and fed via multiple flow routes.
692
693 In semi-arid environments sensitive to water balance changes, epikarst evaporation and
694 disequilibrium fractionation from kinetic effects are likely to lead to ^{18}O enrichment during
695 drier phases. Epikarst evaporation driven fractionation is controlled by changes to water
696 balance and rainfall amount on the surface which has lag times before being expressed in the
697 stalagmite record. This is more important in dry or drought conditions (e.g. Millennium
698 Drought; Figure 6) where storage volumes are low and larger air pockets develop as stores
699 decline (Figure 7). However, the timing of the $\delta^{18}O_{spel.}$ response to dry surface conditions
700 suggests that they are out-of-phase with the actual occurrence of drought periods on the
701 surface (Figure 6; e.g. WB, peak $\delta^{18}O_{spel}$ occurs ~9 years after the end of the WWII Drought).
702 Thus, the interpretation of $\delta^{18}O_{spel}$ represents water balance excursions but lagged due to
703 inertia of the vadose zone in its response to surface climate changes.
704
705 Stalagmites in this study show that $\delta^{18}O_{spel}$ is sensitive to changes in hydroclimate or water
706 balance, resulting in isotopic enrichment as a direct result of drying conditions – thus
707 preserving the isotopic impact of reduced recharge. This differs from a classic direct
708 interpretation of the $\delta^{18}O_{spel}$ as a proxy for rainfall amount. Large modifications of the
709 original $\delta^{18}O_{precip}$ value occurs in this water-limited cave system, from both the karst and the

cave environment, and consequently cave monitoring is essential to ascertain the dominant processes that affect $\delta^{18}O_{spel.}$ The combination of epikarst evaporation and kinetic isotope effects in the cave e.g. resulting from a rapid loss of CO_2 or change in drip interval, are likely to positively shift $\delta^{18}O_{spel}$ in the same direction and thus these disequilibrium stalagmites in dryland environments may be useful as past water balance or paleorecharge records.

The significant flood event affecting most of SE Australia in 1955 CE was recorded in stalagmite WB, suggesting that these stalagmites, because of their sensitivity to water balance changes, may be very suitable archives of extreme pluvials or floods. Rainfall in this region is strongly governed by ENSO, where La Niña's have a more significant influence on the intensity and duration of rainfall events than El Niño's. Thus, paleorecharge records from Wellington Caves would be useful for providing evidence of the frequency and severity of past pluvial and drought periods. Such records may be important in determining paleoprecipitation anomalies and could be used to elucidate the relationship of climatic dynamics with rainfall over SE Australia.

Acknowledgements

Thank you to the Dubbo Regional Council and continued support of cave staff and management at Wellington Caves. Thank you to Dr. Peter Graham for collecting instantaneous rainfall samples and to Dr. Catherine Jex for analysing the rainfall samples. AB, MM and MSA were partly supported by the ARC/NWC National Centre for Groundwater Research and Training. SF acknowledges the support of DP 160101058. The outcomes of this study contribute to ARC Discovery Project DP140102059 awarded to PCT. MOC was supported by the European Community's Seventh Framework Programme

[FP7/2007–2013] under grant agreement No.299091 and by an Independent Research Fellowship from the UK Natural Environment Research Council (NE/P017819/1).

References

Anderson, W. T., Bernasconi, S.M., McKenzie, J.A., and Saurer, M. (1998). Oxygen and carbon isotopic record of climatic variability in tree ring cellulose (Picea abies): An example from central Switzerland (1913–1995). *J. Geophys. Res-Atmos* **103(D24)**, 31625-31636.

Australian Bureau of Statistics (2008) *1301.0 - Yearbook Complete, 2008 Natural Disasters in Australia, Article 4*. Retrieved from: http://www.abs.gov.au/AUSSTATS/abs@.nsf/7d12b0f6763c78caca257061001cc588/fecb2ab6de16171eca2570de0005871b!OpenDocument

Ayalon, A., Bar-Matthews, M. and Sass, E. (1998). Rainfall-recharge relationships within a karstic terrain in the Eastern Mediterranean semi-arid region, Israel: $\delta^{18}O$ and δD characteristics. *J. Hydrol.* **207**, 18-31.

Baker, A., Genty, D., Dreybrodt, W., Barnes, W.L., Mockler, N.J. and Grapes, J., 1998. Testing Theoretically Predicted Stalagmite Growth Rate with Recent Annually Laminated Samples: Implications for Past Stalagmite Deposition. *Geochim. Cosmochim. Acta* **62,** 393-404.

Baker, A., Wilson, R., Fairchild, I.J., Franke, J., Spötl, C., Mattey, D., Trouet, V., and Fuller, L. (2011). High resolution $\delta^{18}O$ and $\delta^{13}C$ records from an annually laminated Scottish stalagmite and relationship with last millennium climate. *Global Planet. Change* **79**, 303-311.

758 Baker, A., Jex, C.N., Rutlidge, H., Woltering, M., Blyth, A.J., Andersen, M.S., Cuthbert,
759 M.O., Marjo, C.E., Markowska, M., Rau, G.C. and Khan, S.J. (2016a). An irrigation
760 experiment to compare soil, water and speleothem tetraether membrane lipid
761 distributions. *Org. Geochem.* **94**, 12-20.
762 Baker, A., Flemons, I., Andersen, M.S., Coleborn, K. and Treble, P.C. (2016b). What
763 determines the calcium concentration of speleothem-forming drip waters? *Global Planet.*
764 *Change* **143**, 152-161.
765 Baker, A., Hartmann, A., Duan, W., Hankin, S., Comas-Bru, L., Cuthbert, M.O., Treble,
766 P.C., Banner, J., Genty, D., Baldini, L., Bartolomé, M., Moreno, A., and Pérez-Mejías,
767 C. Global distribution and controls on cave drip water oxygen isotope composition.
768 *Nature Communications*, **10**, Article number: 2984
769 Baker, A.J., Mattey, D.P. and Baldini, J.U.L. (2014). Reconstructing modern stalagmite
770 growth from cave monitoring, local meteorology, and experimental measurements of
771 dripwater films. *Earth Planet. Sci. Lett.* **392**, 239-249.
772 Bar-Matthews, M., Ayalon, A., Matthews, A., Sass, E. and Halicz, L. (1996). Carbon and
773 oxygen isotope study of the active water-carbonate system in a karstic Mediterranean
774 cave: Implications for paleoclimate research in semiarid regions. *Geochim. Cosmochim.*
775 *Acta* **60**, 337-347.
776 Bar-Matthews, M., Ayalon, A., Gilmour, M., Matthews, A. and Hawkesworth, C.J. (2003).
777 Sea–land oxygen isotopic relationships from planktonic foraminifera and speleothems in
778 the Eastern Mediterranean region and their implication for paleorainfall during
779 interglacial intervals. *Geochim. Cosmochim. Acta* **67**, 3181-3199.
780 Benavente, J., Vadillo, I., Carrasco, F., Soler, A., Liñán, C. and Moral, F. (2010). Air
781 Carbon Dioxide Contents in the Vadose Zone of a Mediterranean Karst. *Vadose Zone J.*
782 **9**, 126-136.

783 Berthelin, R., Rinderer, M., Andreo, B., Baker, A., Kilian, D., Leonhardt, G., Lotz, A.,
784 Lichtenwoehrer, K., Mudarra, M., Padilla, I. Y., Pantoja Agreda, F., Rosolem, R., Vale,
785 A., and Hartmann, A.: A soil moisture monitoring network to characterize karstic
786 recharge and evapotranspiration at five representative sites across the globe, Geosci.
787 Instrum. Method. Data Syst. Discuss., https://doi.org/10.5194/gi-2019-22

788 Bureau of Meteorology (2010). *Rainfall Deciles (AWA grids 1900-pres) February 1955*.
789 Retrieved from: http://www.bom.gov.au/climate/enso/lnlist/195457/195502.gif .

790 Bureau of Meteorology (2011). *Australian Water resources Assessment 2010*. Retrieved
791 from: http://www.bom.gov.au/water/awra/2010/documents/assessment-low.pdf

792 Bureau of Meteorology (2015). *Recent rainfall, drought and southern Australia's long-term*
793 *rainfall decline*. Retrieved from: http://www.bom.gov.au/climate/updates/articles/a010-
794 southern-rainfall-decline.shtml Bureau of Meteorology (2019). *Southern Oscillation*
795 *Index (SOI) since 1876*. Retrieved from:
796 http://www.bom.gov.au/climate/current/soihtm1.shtml

797 Bureau of Meteorology (2019a). *Indian Ocean influences on Australian climate*. Retrieved
798 from: http://www.bom.gov.au/climate/iod/

799 Butterworth, J. A., Schulze, R. E., Simmonds, L. P., Moriarty, P., and Mugabe, F.:
800 Hydrological processes and water resources management in a dryland environment IV:
801 Long-term groundwater level fluctuations due to variation in rainfall, *Hydrol. Earth Syst.*
802 *Sci*., 3, 353–361, https://doi.org/10.5194/hess-3-353-1999, 1999.

803 Cai, Y., Cowan, T., Briggs, P.R. and Raupach, M.R. (2009). Rising temperature depletes soil
804 moisture and exacerbates severe drought conditions across southeast Australia. *Geophys.*
805 *Res. Lett.* **36** L21709.

Christensen, J.H., K. Krishna Kumar, Marshall, G., Turner, J. (2013). Climate Phenomena and their Relevance for Future Regional Climate Change. In: Stocker, T.F., D. Qin, G.-K. Plattner, M. Tignor, S.K. Allen, J. Boschung, A. Nauels, Y. Xia, V. Bex and P.M. Midgley (eds.) *The Physical Science Basis. Contribution of Working Group I to the Fifth Assessment Report of the Intergovernmental Panel on Climate Change 2013*. Cambridge, UK and New York, NY: Cambridge University Press, 1217-1308.

Clarke, H., Lucas, C. and Smith, P. (2013). Changes in Australian fire weather between 1973 and 2010. *Int. J. Climatol.* **33**, 931-944.

Coplen, T.B. (1988). Normalization of oxygen and hydrogen isotope data. *Chem. Geol.: Isotope Geoscience* **72**, 293-297.

Coplen, T.B. (2007). Calibration of the calcite–water oxygen-isotope geothermometer at Devils Hole, Nevada, a natural laboratory. *Geochim. Cosmochim. Acta* **71**, 3948-3957.

Crosbie, R.S., Pickett, T., Mpelasoka, F.S., Hodgson, G., Charles, S.P. and Barron, O.V. (2013). An assessment of the climate change impacts on groundwater recharge at a continental scale using a probabilistic approach with an ensemble of GCMs. *Climatic Change* **117**, 41-53.

Cuthbert, M., Mackay, R. and Nimmo, J. (2013). Linking soil moisture balance and source-responsive models to estimate diffuse and preferential components of groundwater recharge. *Hydrol. Earth Syst. Sci.* **17**, 1003-1019.

Cuthbert, M.O., Baker, A., Jex, C.N., Graham, P.W., Treble, P.C., Andersen, M.S. and Ian Acworth, R. (2014a). Drip water isotopes in semi-arid karst: Implications for speleothem paleoclimatology. *Earth Planet. Sci. Lett.* **395**, 194-204.

Cuthbert, M.O., Rau, G.C., Andersen, M.S., Roshan, H., Rutlidge, H., Marjo, C.E., Markowska, M., Jex, C.N., Graham, P.W., Mariethoz, G., Acworth, R.I. and Baker, A. (2014b). Evaporative cooling of speleothem drip water. *Sci. Rep.* **4**, 5162.

D'Odorico, P. and Porporato, A. (2006). *Dryland Ecohydrology*. New York, NY: Springer-verlag.

Dai, A. (2013). Increasing drought under global warming in observations and models. *Nature Clim. Change* **3**, 52-58.

Dansgaard, W. (1964). Stable isotopes in precipitation. *Tellus* **16**, 436-468.

Day, C.C. and Henderson, G.M. (2011). Oxygen isotopes in calcite grown under cave-analogue conditions. *Geochim. Cosmochim. Acta* **75**, 3956-3972.

Deininger, M., Fohlmeister, J., Scholz, D. and Mangini, A. (2012). Isotope disequilibrium effects: The influence of evaporation and ventilation effects on the carbon and oxygen isotope composition of speleothems – A model approach. *Geochim. Cosmochim. Acta* **96**, 57-79.

Deininger, M. and Scholz, S. (2019). ISOLUTION 1.0: an ISOtope evoLUTION model describing the stable oxygen ($\delta^{18}O$) and carbon ($\delta^{13}C$) isotope values of speleothems. *International Journal of Speleology*, **48**, 21-32.

Denniston, R.F., González, L.A., Asmerom, Y., Baker, R.G., Reagan, M.K. and Bettis, E.A. (1999). Evidence for increased cool season moisture during the middle Holocene. *Geology* **27**, 815-818.

Desmarchelier, J.M., Goede, A., Ayliffe, L.K., McCulloch, M.T. and Moriarty, K. (2000). Stable isotope record and its palaeoenvironmental interpretation for a late Middle Pleistocene speleothem from Victoria Fossil Cave, Naracoorte, South Australia. *Quatern. Sci. Rev.* **19**, 763-774.

Dietzel, M., Tang, J., Leis, A. and Köhler, S.J. (2009). Oxygen isotopic fractionation during inorganic calcite precipitation — Effects of temperature, precipitation rate and pH. *Chem. Geol.* **268**, 107-115.

855 Dreybrodt, W. (1999). Chemical kinetics, speleothem growth and climate. *Boreas* **28**, 347-
856 356.
857 Dreybrodt, W. and Scholz, D. (2011). Climatic dependence of stable carbon and oxygen
858 isotope signals recorded in speleothems: from soil water to speleothem calcite. *Geochim.*
859 *Cosmochim. Acta* **75**, 734-752.
860 Even, H., Carmi, I., Magaritz, M. and Gerson, R. (1986). Timing the transport of water
861 through the upper vadose zone in a Karstic system above a cave in Israel. *Earth Surf.*
862 *Proc. Land.* **11**, 181-191.
863 Fawcett, R.J.B., Trewin, B.C., Braganza, K., Smalley, R.J., Jovanovic, B. and Jones, D.A.
864 (2012). *On the sensitivity of Australian temperature trends and variability to analysis*
865 *methods and observation networks*, *CAWCR Technical Report* (Report no. 050).
866 Aspendale, VIC: The Centre for Australian Weather and Climate Research.
867 Feng, S. and Fu, Q. (2013). Expansion of global drylands under a warming climate. *Atmos.*
868 *Chem. Phys.* **13**, 10081-10094.
869 Fleitmann, D., Burns, S.J., Neff, U., Mudelsee, M., Mangini, A. and Matter, A. (2004).
870 Palaeoclimatic interpretation of high-resolution oxygen isotope profiles derived from
871 annually laminated speleothems from Southern Oman. *Quatern. Sci. Rev.* **23**, 935-945.
872 Friedman, I. and O'Neil, J.R. (1977). *Compilation of stable isotope fractionation factors of*
873 *geochemical interest* (Report no. 440-KK). Washington, DC: U.S. Geological Survey.
874 Frisia, S. (2015). Microstratigraphic logging of calcite fabrics in speleothems as tool for
875 palaeoclimate studies. *Intern. J. Speleology* **44**, 1-16.
876 Frisia, S., Borsato, A and Hellstrom, J. (2018) High spatial resolution investigation of
877 nucleation, growth and early diagenesis in speleothems as exemplar for sedimentary
878 carbonates. *Earth Sci. Rev.* **178**, 68-91.

879 Gonfiantini, R. (1984). *Advisory Group Meeting on Stable Isotope Reference Samples for*
880 *Geochemical and Hydrological Investigations* (Report to the Director General of the
881 International Atomic Energy Agency). Vienna, WIE: IAEA.
882 Gonfiantini, R. (1986). Chapter 3 – Environmental isotopes in lake studies In: Fontes, J.C.
883 (Ed.), *The Terrestrial Environment*, (pp. 113-168). Amsterdam, NH: Elsevier.
884 Hartmann, A. and Baker, A. (2017). Modelling karst vadose zone hydrology and its relevance
885 for paleoclimate reconstruction. *Earth Sci. Rev.* **172**, 178-192.
886 Huang, J., Ji, M., Xie, Y., Wang, S., He, Y. and Ran, J., 2016. Global semi-arid climate
887 change over last 60 years. *Clim. Dynam.* **46**, 1131-1150.
888 Hut, G. (1987). *Consultants' Group Meeting on Stable Isotope Reference Samples for*
889 *Geochemical and Hydrological Investigations*, Report to the Director General of the
890 International Atomic Energy Agency. Vienna, WIE: IAEA.
891 Jex, C.N., Mariethoz, G., Baker, A., Graham, P.W., Andersen, M.S., Acworth, R.I., Edwards,
892 N. and Azcurra, C. (2012). Spatially dense drip hydrological monitoring and infiltration
893 behaviour at the Wellington Caves, South East Australia. *Int. J. Speleol.* **41**, 283-296.
894 Jolly, W.M., Cochrane, M.A., Freeborn, P.H., Holden, Z.A., Brown, T.J., Williamson, G.J.
895 and Bowman, D.M.J.S. (2015). Climate-induced variations in global wildfire danger from
896 1979 to 2013. *Nature Comms.* **6**, 7537.
897 Kaufman, A., Bar-Matthews, M., Ayalon, A. and Carmi, I. (2003). The vadose flow above
898 Soreq Cave, Israel: a tritium study of the cave waters. *J. Hydrol.* **273**, 155-163.
899 Keshavarzi, M., 2017. Assessing hydraulic connection and dissolved organic matter in a karst
900 landscape: Wellington, Australia. Unpublished PhD, UNSW.
901 http://handle.unsw.edu.au/1959.4/59756
902 Kim, S. and O'Neil, J.R. (1997). Equilibrium and nonequilibrium oxygen isotope effects in
903 synthetic carbonates. *Geochim. Cosmochim. Acta* **61**, 3461-3475.

King, A.D., Alexander, L.V. and Donat, M.G. (2013). Asymmetry in the response of eastern Australia extreme rainfall to low-frequency Pacific variability. *Geophys. Res. Lett.* **40**, 2271-2277.

Lange, J., Greenbaum, N., Husary, S., Ghanem, M., Leibundgut, C. and Schick, A.P. (2003). Runoff generation from successive simulated rainfalls on a rocky, semi-arid, Mediterranean hillslope. *Hydrol. Procs.* **17**, 279-296.

Markowska, M., Baker, A., Andersen, M. S., Jex, C. N., Cuthbert, M. O., Rau, Gabriel C., Graham, P. W., Rutlidge, H., Mariethoz, G., Marjo, C. E., Treble, Pauline C., and Edwards, N. (2016). Semi-arid zone caves: Evaporation and hydrological controls on $\delta^{18}O$ drip water composition and implications for speleothem paleoclimate reconstructions. *Quatern. Sci. Rev.* **131**, 285-301.

Markowska, M., Fohlmeister, J., Treble, P.C., Baker, A., Andersen, M.S. and Hua, Q. (2019). Modelling the 14C bomb-pulse in young speleothems using a soil carbon continuum model, *Geochim. Cosmochim. Acta*, doi.org/10.1016/j.gca.2019.04.029

Mattey, D., Lowry, D., Duffet, J., Fisher, R., Hodge, E. and Frisia, S. (2008). A 53 year seasonally resolved oxygen and carbon isotope record from a modern Gibraltar speleothem: reconstructed drip water and relationship to local precipitation. *Earth Planet. Sci. Lett.* **269**, 80-95.

Mattey, D.P., Fairchild, I.J., Atkinson, T.C., Latin, J.-P., Ainsworth, M. and Durell, R. (2010). Seasonal microclimate control of calcite fabrics, stable isotopes and trace elements in modern speleothem from St Michaels Cave, Gibraltar. *Geol. Soc. Spec. Publ.* **336**, 323-344.

Mattey, D.P., Fisher, R., Atkinson, T.C., Latin, J.P., Durrell, R., Ainsworth, M., Lowry, D. and Fairchild, I.J. (2013). Methane in underground air in Gibraltar karst. *Earth Planet. Sci. Lett.* **374**, 71-80.

McDonough, L.K., Iverach, C.P., Beckmann, S., Manefield, M., Rau, G.C., Baker, A. and Kelly, B.F.J. (2016). Spatial variability of cave-air carbon dioxide and methane concentrations and isotopic compositions in a semi-arid karst environment. *Environ. Earth Sci.* **75**, 1-20.

Mickler, P.J., Stern, L.A. and Banner, J.L. (2006). Large kinetic isotope effects in modern speleothems. *Geol. Soc. Am. Bull.* **118**, 65-81.

Moquet, J.S., Cruz, F.W., Novello, V.F., Stríkis, N.M., Deininger, M., Karmann, I., Santos, R.V., Millo, C., Apaestegui, J., Guyot, J.L., Siffedine, A., Vuille, M., Cheng, H., Edwards, R.L. and Santini, W. (2016). Calibration of speleothem δ18O records against hydroclimate instrumental records in Central Brazil. *Global Planet. Change* **139**, 151-164.

Morgan, K., Jankowski, J. and Taylor, G. (2006). Structural controls on groundwater flow and groundwater salinity in the Spicers Creek catchment, Central West region, New South Wales. *Hydrol. Procs.* **20**, 2857-2871.

Mühlinghaus, C., Scholz, D. and Mangini, A. (2007). Modelling stalagmite growth and δ13C as a function of drip interval and temperature. *Geochim. Cosmochim. Acta* **71**, 2780-2790.

Mühlinghaus, C., Scholz, D. and Mangini, A. (2009). Modelling fractionation of stable isotopes in stalagmites. *Geochim. Cosmochim. Acta* **73**, 7275-7289.

Murphy, B.F. and Timbal, B. (2008). A review of recent climate variability and climate change in southeastern Australia. *Int. J. Clim.* **28**, 859-879.

NCC & BoM: National Climate Centre, Bureau of Meteorology (2011). *Frequent heavy rain events in late 2010/early 2011 lead to widespread flooding across eastern Australia*. Special Climate Statement 24. Retrieved form: http://www.bom.gov.au/climate/current/statements/scs24b.pdf

953 Nicholls, N. (2010). Local and remote causes of the southern Australian autumn-winter
954 rainfall decline, 1958–2007. *Clim. Dyn.* **34**, 835-845.
955 Pittock, B., Abbs, D., Suppiah, R. and Jones, R. (2006). Climatic Background to Past and
956 Future Floods in Australia, *Adv. Ecol. Res.* ***39***,13-39.
957 Rau, G.C., Cuthbert, M.O., Andersen, M.S., Baker, A., Rutlidge, H., Markowska, M.,
958 Roshan, H., Marjo, C.E., Graham, P.W. and Acworth, R.I. (2015). Controls on cave drip
959 water temperature and implications for speleothem-based paleoclimate reconstructions.
960 *Quatern. Sci. Rev.* **127**, 19-36.
961 Raupach, M.R., Briggs, P.R., Haverd, V., King, E.A., Paget, M. and Trudinger, C.M. (2009).
962 *Australian Water Availability Project (AWAP): CSIRO Marine and Atmospheric*
963 *Research Component: Final Report for Phase 3* (CAWCR Technical Report 013),
964 Canberra, ACT: CSIRO.
965 Raupach, M.R., Briggs, P.R., Haverd, V., King, E.A., Paget, M. and Trudinger, C.M. (2012).
966 *Australian Water Availability Project*. CSIRO Marine and Atmospheric Research.
967 Retrieved from: http://www.csiro.au/awap
968 Rozanski, K., Araguás-Araguás, L. and Gonfiantini, R. (1993). *Isotopic Patterns in Modern*
969 *Global Precipitation, Climate Change in Continental Isotopic Records*. Washington, DC:
970 American Geophysical Union.
971 Rutlidge, H., Baker, A., Marjo, C.E., Andersen, M.S., Graham, P.W., Cuthbert, M.O., Rau,
972 G.C., Roshan, H., Markowska, M., Mariethoz, G. and Jex, C.N. (2014). Dripwater
973 organic matter and trace element geochemistry in a semi-arid karst environment:
974 Implications for speleothem paleoclimatology. *Geochim. Cosmochim. Acta* **135**, 217-230.
975 Rutlidge, H., Andersen, M.S., Baker, A., Chinu, K.J., Cuthbert, M.O., Jex, C.N., Marjo, C.E.,
976 Markowska, M. and Rau, G.C. (2015). Organic characterisation of cave drip water by LC-
977 OCD and fluorescence analysis. *Geochim. et Cosmochim. Acta* **166**, 15-28.

978 Scholz, D., Mühlinghaus, C. and Mangini, A., 2009. Modelling δ13C and δ18O in the
979 solution layer on stalagmite surfaces. *Geochim. Cosmochim. Acta* **73**, 2592- 2602.
980 Scholz, D., Frisia, S., Borsato, A., Spötl, C., Fohlmeister, J., Mudelsee, M., Miorandi, R. and
981 Mangini, A. (2012). Holocene climate variability in north-eastern Italy: potential
982 influence of the NAO and solar activity recorded by speleothem data. *Clim. Past* **8**, 1367-
983 1383.
984 Sheffer, N.A., Cohen, M., Morin, E., Grodek, T., Gimburg, A., Magal, E., Gvirtzman, H.,
985 Nied, M., Isele, D. and Frumkin, A. (2011). Integrated cave drip monitoring for epikarst
986 recharge estimation in a dry Mediterranean area, Sif Cave, Israel. *Hydrol. Process.* **25**,
987 2837-2845.
988 STAP (2010) Report of the Scientific and Technical Advisory Panel to the Fourth GEF
989 Assembly. Accessed at: https://www.thegef.org/sites/default/files/council-meeting-
990 documents/GEF-A.4-3_-_Report_of_STAP_0_1.pdf
991 Thorpe, E.W. and Tweedie, A.D. (1956). The N.S.W. floods of February 1955. *Aust. Geogr.*
992 **6**, 3-13.
993 Trabucco, A. and Zomer, R.J. (2009). Global Aridity Index (Global-aridity) and Global
994 Potential Evapo-transpiration (Global-PET) Geospatial Database. CGIAR Consortium for
995 Spatial Information. Available from the CGIAR-CSI GeoPortal at
996 http://www.csi.cgiar.org/.
997 Treble, P.C., Budd, W.F., Hope, P.K. and Rustomji, P.K. (2005). Synoptic-scale climate
998 patterns associated with rainfall $\delta^{18}O$ in southern Australia. *J. Hydrol.* 302, 270-282.
999 Treble, P.C., Fairchild, I.J., Baker, A., Meredith, K.T., Andersen, M.S., Salmon, S.U.,
1000 Bradley, C., Wynn, P.M., Hankin, S.I., Wood, A. and McGuire, E. (2016). Roles of forest
1001 bioproductivity, transpiration and fire in a nine-year record of cave dripwater chemistry
1002 from southwest Australia. *Geochim. Cosmochim. Acta* **184**, 132-150.

1003 Trewin, B. (2013). A daily homogenized temperature data set for Australia. *Int. J. Clim.* **33**,
1004 1510-1529.
1005 Ummenhofer, C.C., Sen Gupta, A., Briggs, P.R., England, M.H., McIntosh, P.C., Meyers,
1006 G.A., Pook, M.J., Raupach, M.R. and Risbey, J.S. (2011). Indian and Pacific Ocean
1007 Influences on Southeast Australian Drought and Soil Moisture. *J. Clim.* **24**, 1313-1336.
1008 Van Dijk, A.I.J.M., Beck, H.E., Crosbie, R.S., de Jeu, R.A.M., Liu, Y.Y., Podger, G.M.,
1009 Timbal, B. and Viney, N.R. (2013). The Millennium Drought in southeast Australia
1010 (2001– 2009): Natural and human causes and implications for water resources,
1011 ecosystems, economy, and society. *Wat. Res. Res.* **49**, 1040-1057.
1012 Verdon-Kidd, D.C. and Kiem, A.S. (2009). Nature and causes of protracted droughts in
1013 southeast Australia: Comparison between the Federation, WWII, and Big Dry droughts.
1014 *Geophys. Res. Lett.* **36**, L22707.
1015 Walker, B. (2010). Dubbo's big flood, gone but not forgotten, *Daily Liberal*. Retrieved from:
1016 http://www.dailyliberal.com.au/story/855359/dubbos-big-flood-gone-but-not-forgotten/
1017 Weber, K., Stewart, M. (2004). A Critical Analysis of the Cumulative Rainfall Departure
1018 Concept. *Groundwater*. **42** (6); 935-938.
1019 Williamson, G., J., Prior, L., D., Jolly, W.M., Cochrane, M., A., Murphy, B., P., Bowman,
1020 D.M.J.S. (2016). Measurement of inter- and intra-annual variability of landscape fire
1021 activity at a continental scale: the Australian case. *Environ. Res. Lett.* **11**, 035003.

Figure Captions

Figure 1. Aridity map of Australia compiled with spatial aridity data from Trabucco and Zomer (2009). The location of Wellington is shown.

Figure 2. Climate variables over 1930 – 2010 CE. Panels A and B show the monthly maximum and minimum temperature anomalies, respectively, derived from the Australian Water Availability Project (AWAP) (Raupach et al., 2009, 2012) using a 13-point box averaging algorithm and a 96-point smoothing (black line). Panel C shows AWAP-derived monthly PE with a 6-point box smoothing. Panel D shows monthly deep drainage (recharge) from AWAP data. Panel E is the annual rainfall from Bureau of Meteorology (Wellington, station ID: 065034) with the thick blue line showing the 9-point box smoothing. Panel F shows the monthly cumulative rainfall departure (black line) calculated from Bureau of Meteorology rainfall data (station ID: 065034); seasonal rainfall departure, where DJF represents summer months, MAM represents autumn months, JJA represents winter months and SON represents spring months. The period of stalagmite growth for WB (green) and WC (orange) are also shown in Panel G at the bottom of the figure.

Figure 3. Upper panel shows cross-section of stalagmite WB (Panel A) and WC (Panel B); The sampling transects are indicated in panels C (stalagmite WB) and D (stalagmite WC) and the $\delta^{18}O$ time series overlain on calcite fabric in panels E (stalagmite WB) and F (stalagmite WC). The photographs in the lower panels show a microscope image of the WB flood layer (Panel G); the UV fluorescence microscope (365 nm) image of WB microsparite layers at the top of the panel before the flood (Panel H); the Ziess microscope image of WB top layers

(Panel I) and microsparite layers below the flood (Panel J); and the surface above Cathedral Cave showing the relative positions of 'WB' and 'WC' (Panel K).

Figure 4. Rainfall $\delta^{18}O$ versus δD with the local meteoric waterline (black), precipitation-weighted mean annual rainfall (yellow diamond), monthly-integrated rainfall (red stars), small volume event rainfall < 5 mm samples (blue triangles) and large volume (> 45mm) event rainfall samples (blue circles).

Figure 5. Time series of stalagmite WB $\delta^{18}O$ (Panel A) and $\delta^{13}C$ (Panel B) and timeseries of of WC $\delta^{18}O$ (Panel C) and $\delta^{13}C$ (Panel D). Scatterplots of stalagmite WB $\delta^{18}O$ vs. $\delta^{13}C$ showing $r^2 = 0.00$ (Panel E) and WC $\delta^{18}O$ vs. $\delta^{13}C$ (Panel F) showing $r^2 = 0.77$. 3-year box-smoothing was applied to the time series, shown by the "Trend" (red line). The blue background behind each $\delta^{18}O_{spel}$ time series shows the range (-0.13 to -5.53 ‰ VPDB) of calculated calcite from the temperature dependent fractionation equation in Kim and O'Niel (1997) for the measured drip water values from South Passage from Cuthbert et al. (2014). ^{14}C bomb-pulse age and Organic Carbon models presented in Markowska et al. (2019) were used to build chronologies for stalagmites WB and WC, respectively.

Figure 6. Coeval $\delta^{18}O$ stalagmite records compared to the instrumental record. Panel A shows the IOD phases with positive (red rectangles) and negative phases (blue rectangles) (BoM, 2019a); Panel B shows the positive SOI anomalies (La Niña phases; green) and negative SOI anomalies (El Niño phases; yellow) based on the standardised anomaly of the Mean Sea Level Pressure difference between Tahiti and Darwin according to the Australian Bureau of Meteorology Convention (BoM, 2019); Panel C shows the Monthly Cumulative Rainfall

Deficit (CRD) (thick black line); Winter CRD (blue line); Panel D shows the water excess (precipitation (P) – evapotranspiration(ET)) (mm/d) with mean annual P-ET (thick black line); Panel E shows WB stalagmite $\delta^{18}O$ (red squares) and WC stalagmite $\delta^{18}O$ (black circles) alongside modelled recharge events (deep drainage (blue), from AWAP). The Millennium Drought and WWII Drought are outlined in red and two short droughts (1965-1968 CE and 1982-1983 CE) in yellow. Two significant water excess periods are highlighted in blue (1950-1952 CE and 1955-1956 CE). Numbers 1-6 correspond to peaks in WC $\delta^{18}O_{spel}$ (black) and annual water deficits (yellow), respectively.

Figure 7. Conceptual model of Cathedral Cave over wet and dry hydrological periods using stalagmites WC and WB as examples. Stalagmite WB is connected to a larger storage reservoir than WC, which buffers the response effects of dry periods.

Figure 8. Modelled versus measured $\delta^{18}O$ for stalagmites WB and WC. The age model uncertainty is delineated by the red error bars for an example sample point.

Figure 9. Model output showing the sensitivity of variables water storage depth below which epikarst evaporation occurs , or the volume where epikarst evaporation 'switches on' or becomes important (S2lim, mm) versus the epikarst evaporation rate (mm/d) and the resultant offset in $\delta^{18}O$ due to epikarst evaporation. Assuming that our 1D model store approximates to the actual 3-dimensional karst void, then the likelihood of discontinuous growth is higher when S2lim increases.

Figure 1 revised 191204

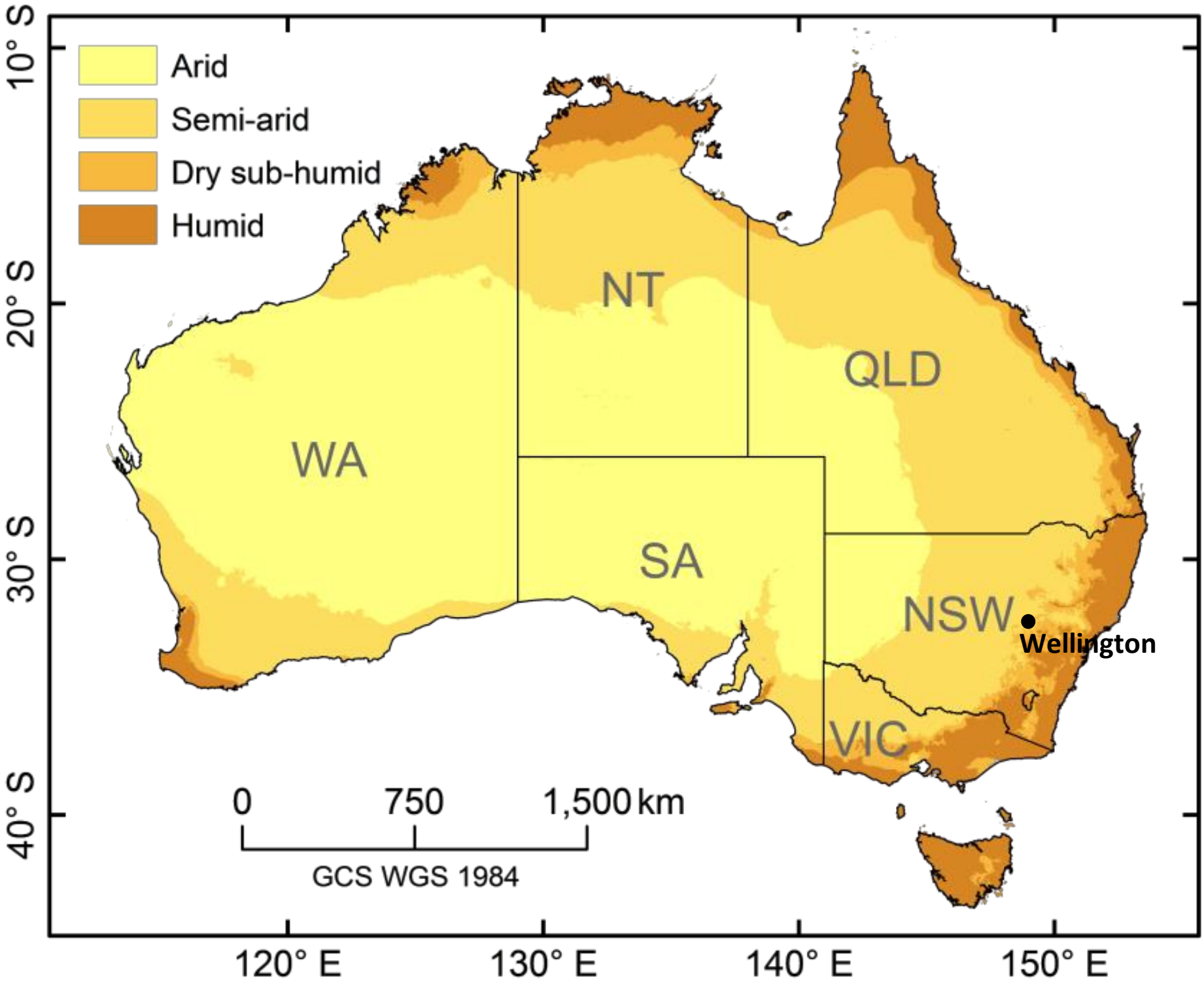

Figure 2 revised 191204

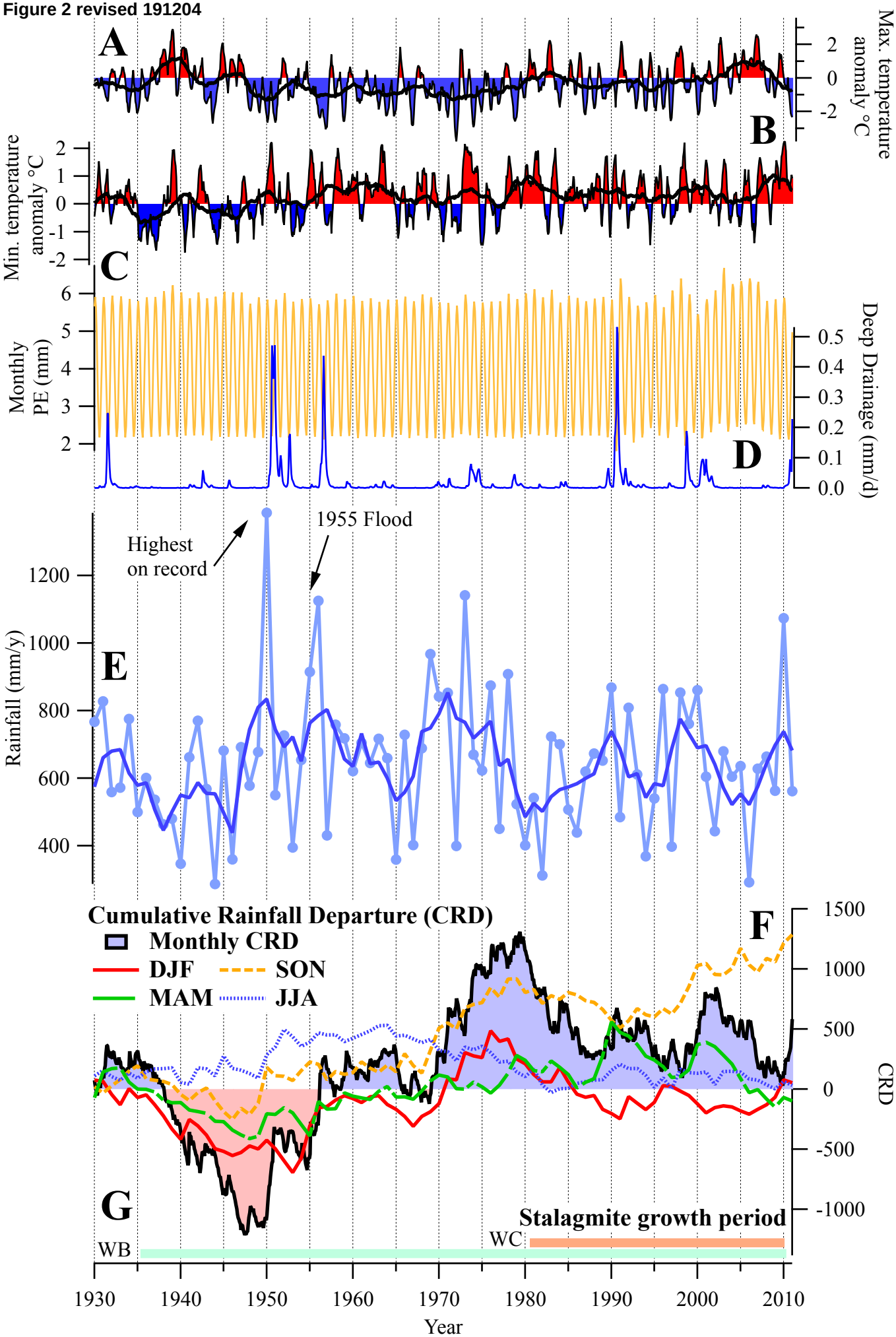

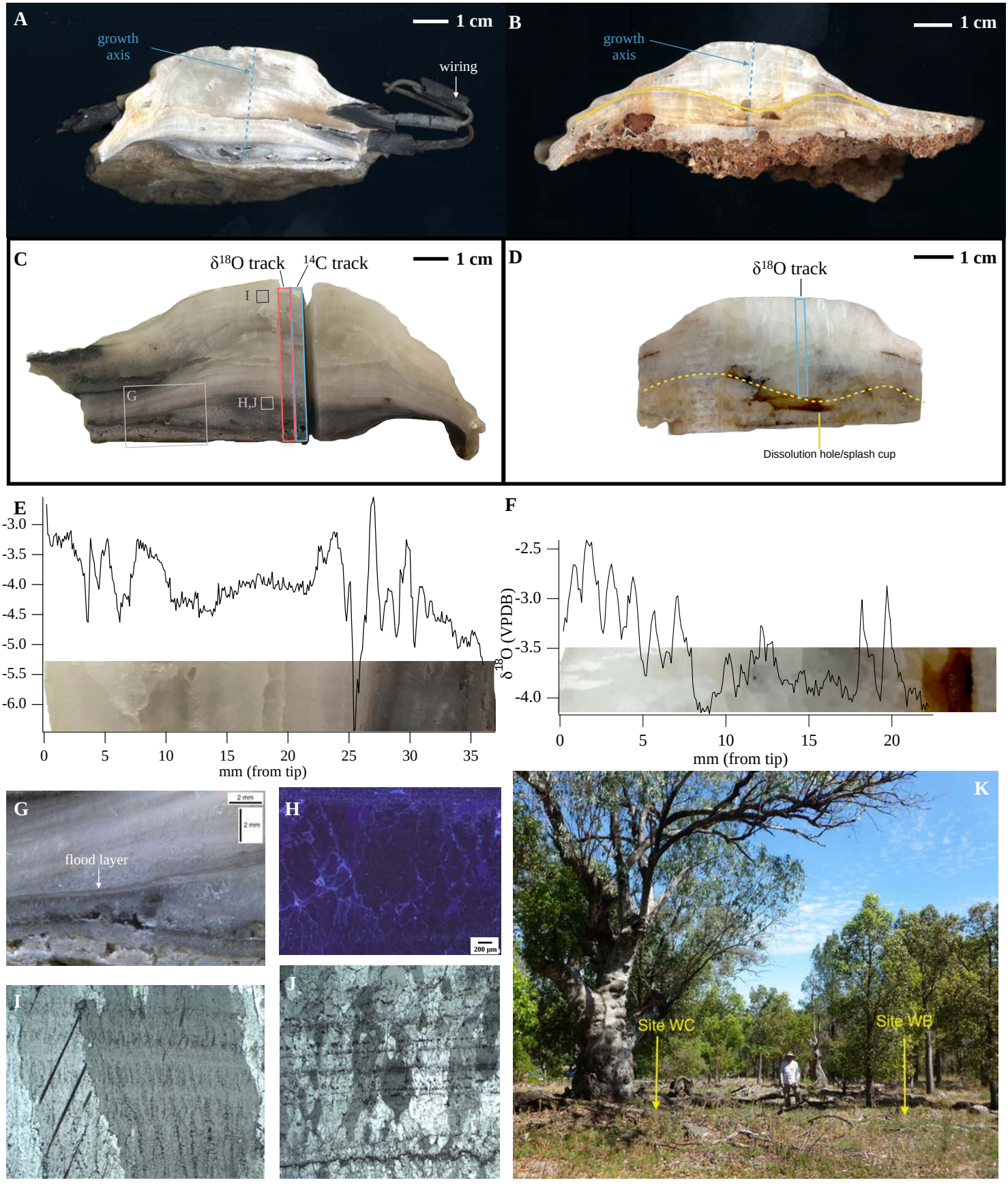
A
1 cm
growth axis
wiring
B
1 cm
growth axis
C
δ18O track
14C track
1 cm
I
G
H,J
D
δ18O track
1 cm
Dissolution hole/splash cup
E
δ18O (VPDB)
-3.0
-3.5
-4.0
-4.5
-5.0
-5.5
-6.0
0
5
10
15
20
25
30
35
mm (from tip)
F
δ18O (VPDB)
-2.5
-3.0
-3.5
-4.0
0
5
10
15
20
mm (from tip)
G
2 mm
flood layer
H
200 µm
I
J
K
Site WC
Site WB

Figure 4

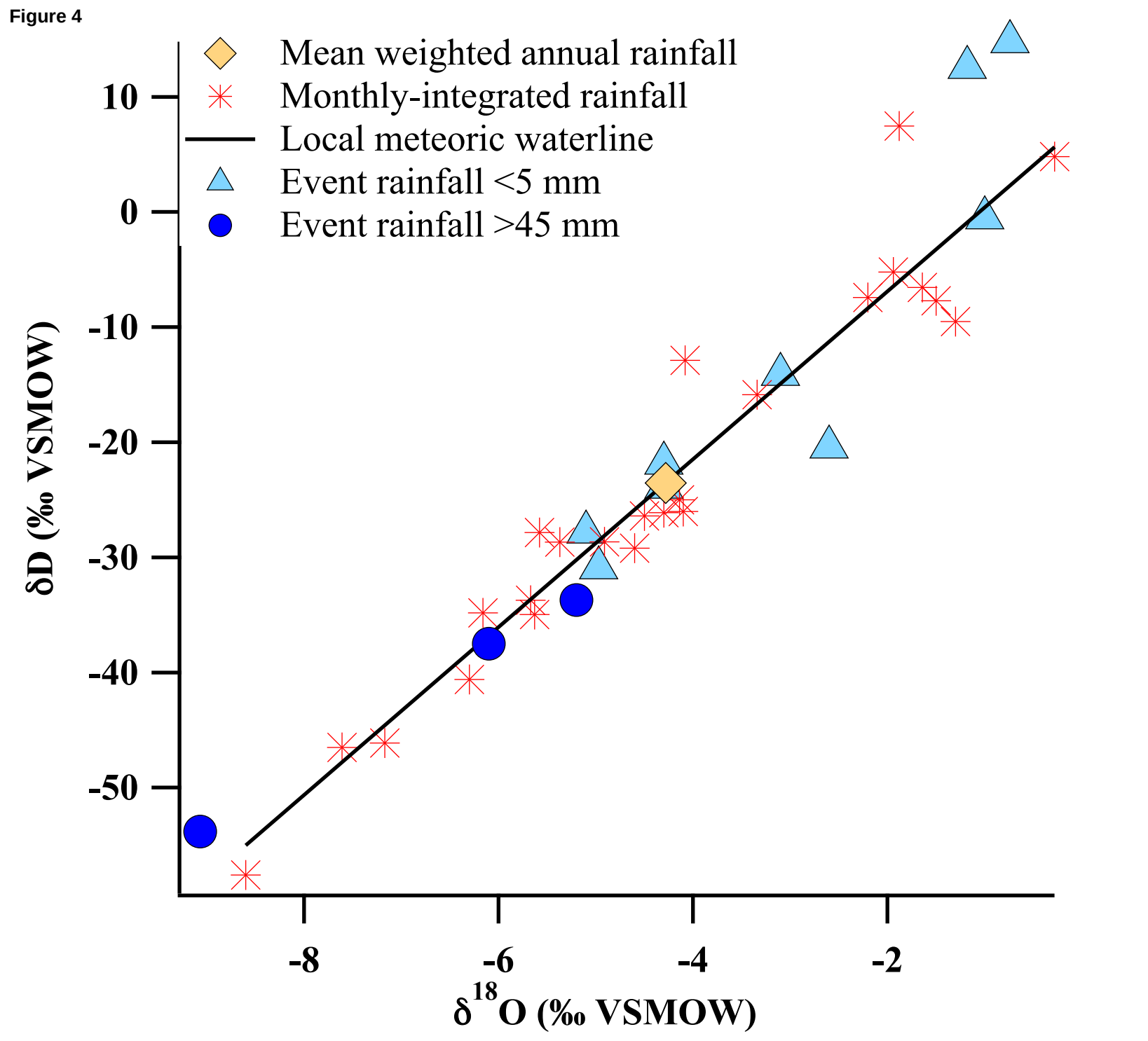
Mean weighted annual rainfall
Monthly-integrated rainfall
Local meteoric waterline
Event rainfall <5 mm
Event rainfall >45 mm
10
0
-10
-20
-30
-40
-50
δD (‰ VSMOW)
-8
-6
-4
-2
δ18O (‰ VSMOW)

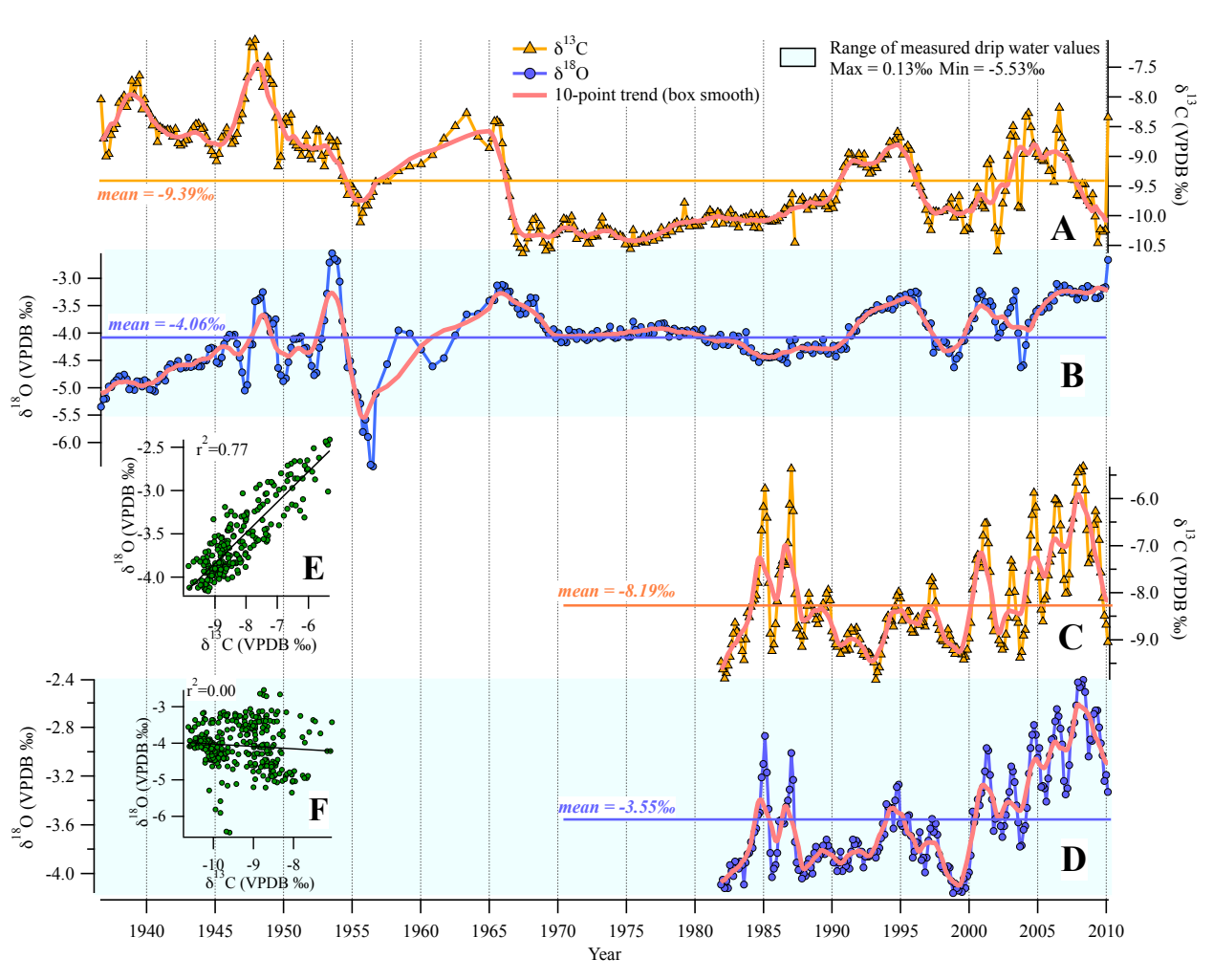
δ13C
δ18O
10-point trend (box smooth)
Range of measured drip water values
Max = 0.13‰ Min = -5.53‰
mean = -9.39‰
mean = -4.06‰
mean = -8.19‰
mean = -3.55‰
A
B
C
D
E
F
r2=0.77
r2=0.00
δ18O (VPDB ‰)
δ13C (VPDB ‰)
Year

Figure 6

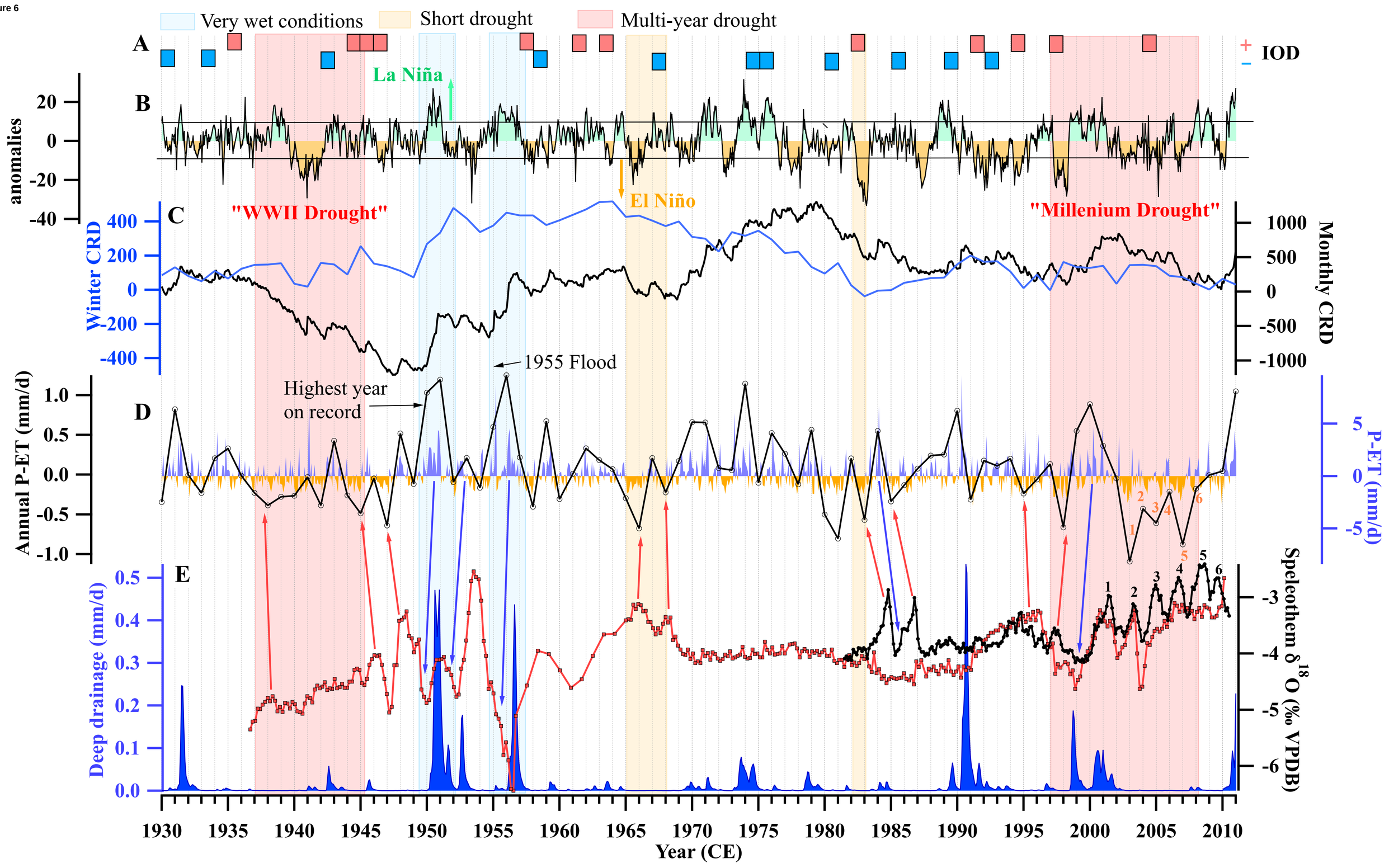
Very wet conditions
Short drought
Multi-year drought
A
IOD
+
−
La Niña
B
SOI anomalies
20
0
-20
-40
El Niño
C
"WWII Drought"
"Millenium Drought"
Winter CRD
400
200
0
-200
-400
1000
500
0
-500
-1000
Monthly CRD
1955 Flood
Highest year on record
D
Annual P-ET (mm/d)
1.0
0.5
0.0
-0.5
-1.0
P-ET (mm/d)
5
0
-5
1
2
3
4
5
6
E
Deep drainage (mm/d)
0.5
0.4
0.3
0.2
0.1
0.0
Speleothem δ18O (‰ VPDB)
-3
-4
-5
-6
1930
1935
1940
1945
1950
1955
1960
1965
1970
1975
1980
1985
1990
1995
2000
2005
2010
Year (CE)

Controls on speleothem $\delta^{18}O$ in drylands caves: Example from Cathedral Cave, SE Australia

Wet conditions

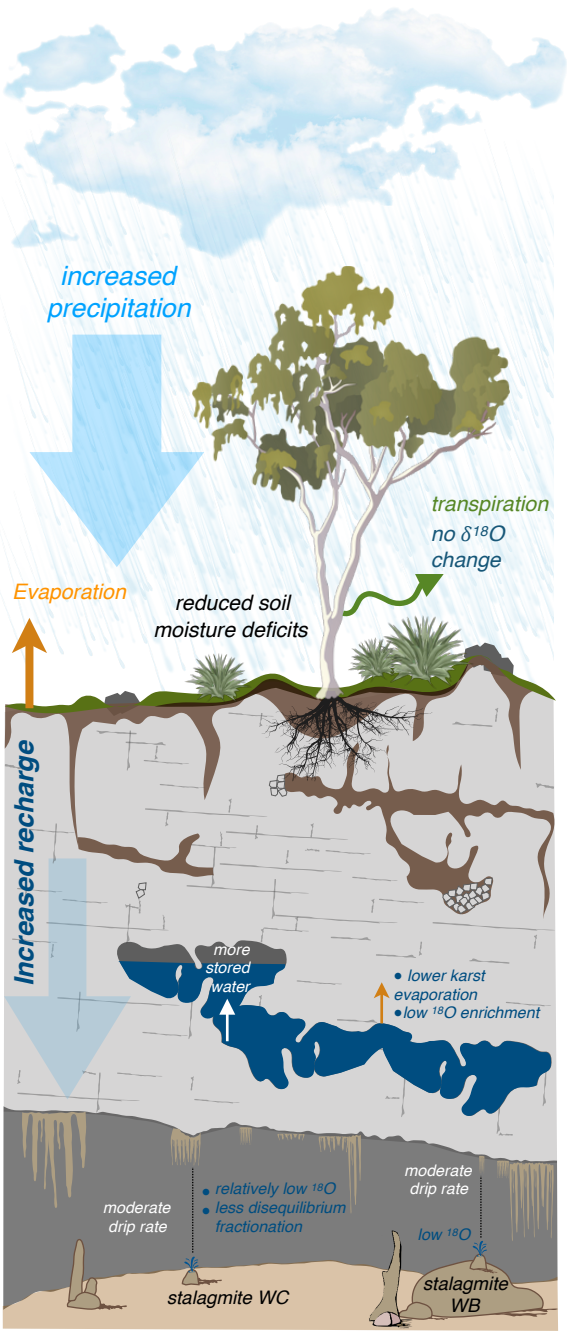

Dry conditions

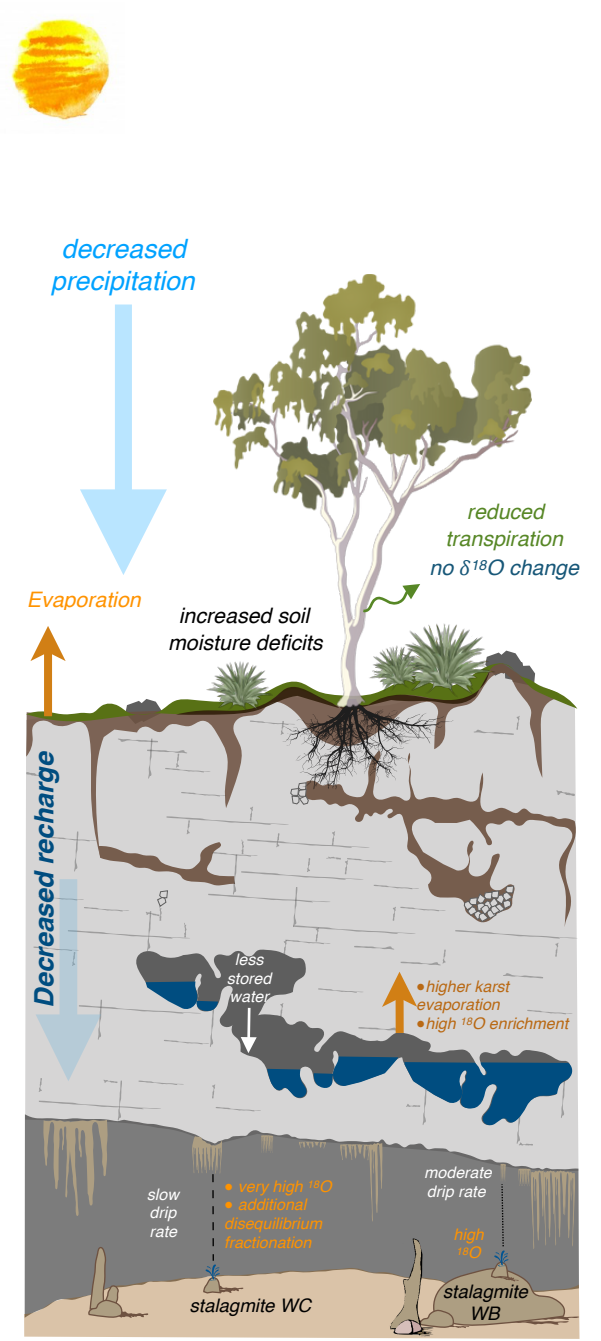

Figure 8

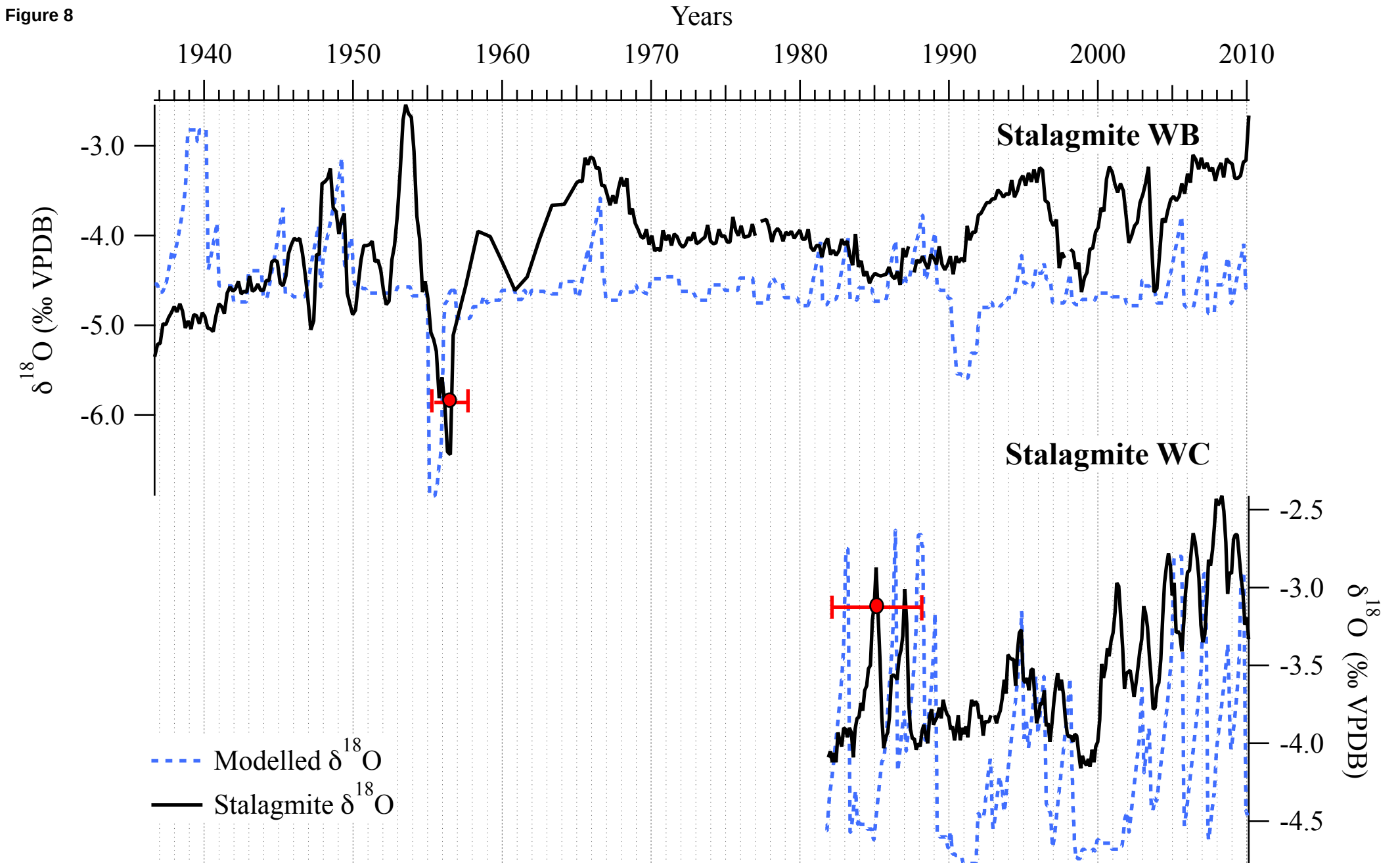
Years
1940
1950
1960
1970
1980
1990
2000
2010
Stalagmite WB
-3.0
-4.0
-5.0
-6.0
δ18O (‰ VPDB)
Stalagmite WC
-2.5
-3.0
-3.5
-4.0
-4.5
δ18O (‰ VPDB)
Modelled δ18O
Stalagmite δ18O

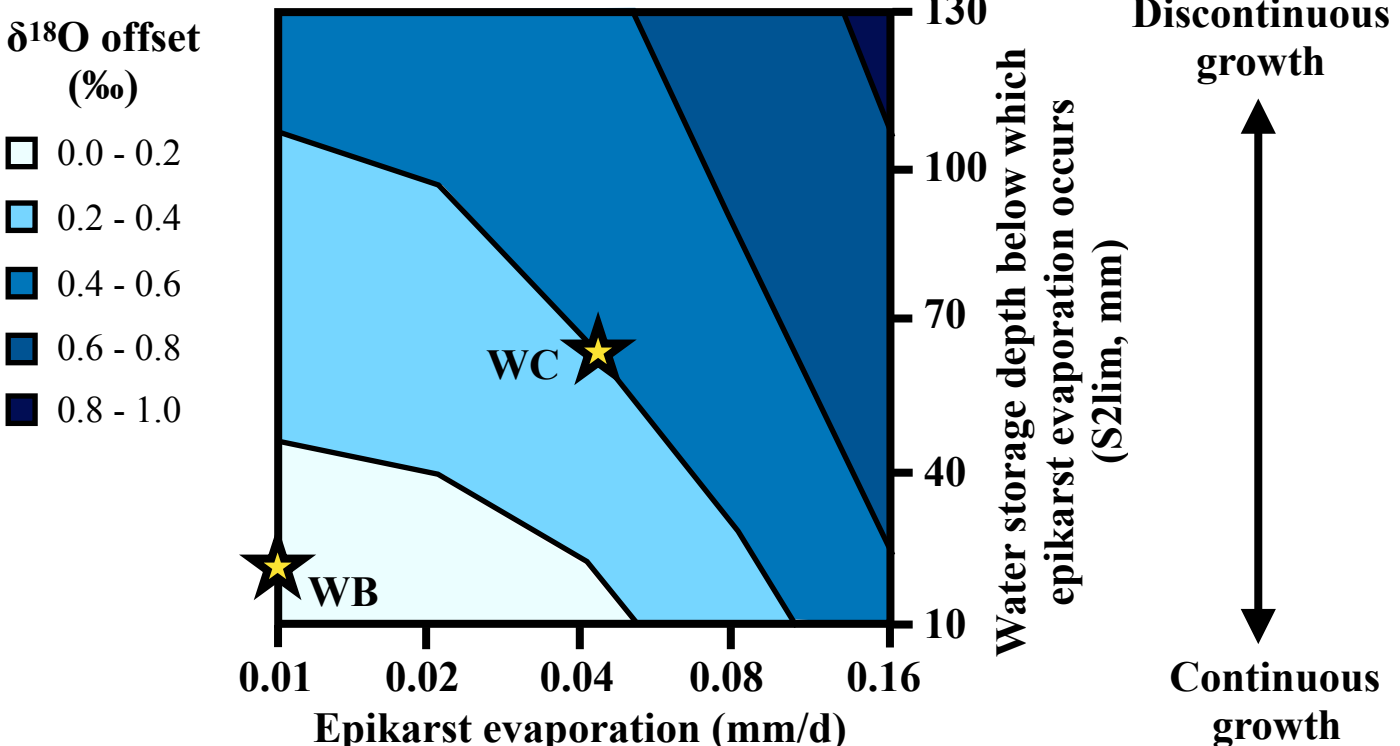
δ18O offset (‰)
0.0 - 0.2
0.2 - 0.4
0.4 - 0.6
0.6 - 0.8
0.8 - 1.0
WC
WB
130
100
70
40
10
Water storage depth below which epikarst evaporation occurs (S2lim, mm)
0.01
0.02
0.04
0.08
0.16
Epikarst evaporation (mm/d)
Discontinuous growth
Continuous growth

Appendix

Click here to download Appendix: Appendix - Figure S1 S2 S3.pdf

Source or Other Companion File Example climate input

Click here to download Source or Other Companion File: Model_Climate_Input.xlsx

Source or Other Companion File model output calcite conversion

Click here to download Source or Other Companion File: Calcite conversion.xlsx

MATLAB File (.fig, .m)

Click here to download MATLAB File (.fig, .m): Isotope_FAO_SMBM_Markowskaetal_GCA2019.m

***Declaration of Interest Statement**

Declaration of interests

☒ The authors declare that they have no known competing financial interests or personal relationships that could have appeared to influence the work reported in this paper.

☐The authors declare the following financial interests/personal relationships which may be considered as potential competing interests: